

ARTICLE TYPE

Constraining the Physical Parameters of Blazars Using the Seed Factor Approach

Chang-Bin Deng,^{1,2} Yong-You Shi,^{3,2} Yu-Jie Song,³ Rui Xue,¹ Lei-Ming Du,³ Ze-Rui Wang,⁴ and Zhao-Hua Xie³¹Department of Physics, Zhejiang Normal University, Jinhua 321004, People's Republic of China²These authors contributed equally to this work.³Department of Physics, Yunnan Normal University, Kunming 650500, People's Republic of China⁴College of Physics and Electronic Engineering, Qilu Normal University, Jinan 250200, People's Republic of China

Author for correspondence: Rui Xue, Lei-Ming Du, Ze-Rui Wang, Email: ruixue@zjnu.edu.cn, duleiming@ynnu.edu.cn, zerui_wang62@163.com.

Abstract

The discovery that blazars dominate the extra-galactic γ -ray sky is a triumph in the *Fermi* era. However, the exact location of γ -ray emission region still remains in debate. Low-synchrotron-peaked blazars (LSPs) are estimated to produce high-energy radiation through the external Compton process, thus their emission regions are closely related to the external photon fields. We employed the *seed factor approach* proposed by Georganopoulos et al. It directly matches the observed seed factor of each LSP with the characteristic seed factors of external photon fields to locate the γ -ray emission region. A sample of 1138 LSPs with peak frequencies and peak luminosities was adopted to plot a histogram distribution of observed seed factors. We also collected some spectral energy distributions (SEDs) of historical flare states to investigate the variation of γ -ray emission region. Those SEDs were fitted by both quadratic and cubic functions using the Markov-chain Monte Carlo method. Furthermore, we derived some physical parameters of blazars and compared them with the constraint of internal $\gamma\gamma$ -absorption. We find that dusty torus dominates the soft photon fields of LSPs and most γ -ray emission regions of LSPs are located at 1–10 pc. The soft photon fields could also transition from dusty torus to broad line region and cosmic microwave background in different flare states. Our results suggest that the cubic function is better than the quadratic function to fit the SEDs.

Keywords: radiation mechanisms: non-thermal – galaxies: jets – gamma-rays: general**1. Introduction**

Blazars are the most extreme subclass of active galactic nuclei (AGN) with a relativistic jet pointing at the Earth (Urry and Padovani 1995). Due to the beaming effect, they have high luminosity, fast variability and variable polarization (Urry and Padovani 1995). According to the equivalent width (EW) of the emission lines, blazars are divided into flat spectrum radio quasars (FSRQs) with $EW \geq 5 \text{ \AA}$ and BL Lacertae objects (BL Lacs) with $EW < 5 \text{ \AA}$, respectively (Urry and Padovani 1995). In the $\log \nu$ - $\log \nu F(\nu)$ diagram, the non-thermal emission from jets dominates blazars' spectral energy distribution (SED), which usually shows a structure of double humps (Marscher et al. 1995). Generally speaking, the low-energy hump is caused by synchrotron radiation of relativistic electrons moving in the magnetic field (Marscher and Gear 1985). Based on the peak frequency of the low-energy hump, blazars are divided into low-synchrotron-peaked (LSP; i.e., $\nu_p^S < 10^{14} \text{ Hz}$), intermediate-synchrotron-peaked (ISP; i.e., $10^{14} < \nu_p^S < 10^{15} \text{ Hz}$), high-synchrotron-peaked (HSP; i.e., $\nu_p^S > 10^{15} \text{ Hz}$), and extreme high-synchrotron-peaked (EHSP; i.e., $\nu_p^S > 10^{17} \text{ Hz}$) blazars (Padovani and Giommi 1995; Costamante et al. 2001; Abdo, Ackermann, Agudo, et al. 2010a). In the leptonic model, the high-energy hump is attributed to the inverse Compton scattering (IC) from the same population of relativistic electrons that emit the synchrotron emission. The seed photons for the IC process could be from the synchrotron radiation

(synchrotron self-Compton, SSC; e.g., Maraschi, Ghisellini, and Celotti 1992; Tavecchio, Maraschi, and Ghisellini 1998) or from external photon fields (external-Compton, EC; e.g., Dermer and Schlickeiser 1993; Sikora, Begelman, and Rees 1994; Błażejowski et al. 2000). In addition, some hadronic models have been proposed to explain the high-energy hump (Aharonian 2000; Böttcher et al. 2013; Xue, Wang, and Li 2022).

Since the launch of the *Fermi*-Large Area Telescope (*Fermi*-LAT) in 2008, high-energy astrophysics has undergone a transformative *Fermi* era marked by profound discoveries (Abdo, Ackermann, Ajello, Allafort, Antolini, Atwood, Axelsson, Baldini, Ballet, Barbiellini, Bastieri, Baughman, Bechtol, Bellazzini, Belli, et al. 2010; Abdo, Ackermann, Ajello, Allafort, Antolini, Atwood, Axelsson, Baldini, Ballet, Barbiellini, Bastieri, Baughman, Bechtol, Bellazzini, Berenji, et al. 2010; Abdo, Ackermann, Ajello, Antolini, et al. 2010). Though nearly 20% LSPs were out of detection, it was found that the diffuse extra-galactic γ -ray background is significantly dominated by emission from blazars (Ajello et al. 2015; Ackermann et al. 2016; Arsioli and Polenta 2018). However, the exact location of γ -ray emission region is still on debate (Agudo et al. 2012; W. Hu et al. 2017; Arsioli and Chang 2018; Tan et al. 2020). Generally speaking, the γ -ray emission of FSRQs is interpreted by the EC process, since strong ambient photon fields are detected (Madejski and Sikora 2016; Huang et al. 2022). The LSP BL Lacs (LBLs) have similar SEDs to those of FSRQs and occasionally show weak emission lines,

therefore, the γ -ray emission of LBLs can also be interpreted by the EC process (Madejski and Sikora 2016; H.-B. Hu *et al.* 2024). For LSPs whose high-energy emission originates from the EC process, investigating the dominant soft photon fields could help to locate the γ -ray emission region. If the γ -ray emission region resides at the base of the jet, the soft photons should be dominated by the accretion disc and the hot corona (Dermer and Schlickeiser 1993; Dermer *et al.* 2009; Rui Xue *et al.* 2021). When the γ -ray emission region is positioned at sub-pc from the central supermassive black hole (SMBH), the soft photons predominantly originate from the broad line region (BLR; $R_{\text{BLR}} \approx 0.1$ pc; Sikora, Begelman, and Rees 1994; Kaspi *et al.* 2007; Bentz *et al.* 2009; Nalewajko, Begelman, and Sikora 2014). On the other hand, if the dissipation of the γ -ray emission occurs at about 1–10 pc, the dominant soft photon source becomes the dusty torus (DT; $R_{\text{DT}} \approx 2.5$ pc; Sikora, Moderski, and Madejski 2008; Zhang *et al.* 2024). In cases where the γ -ray emission region is located in the extended jet, additional external photon fields, such as the cosmic microwave background (CMB) and starlight, play a significant role (Böttcher, Dermer, and Finke 2008; Potter and Cotter 2013a, 2013b, 2013c).

To pinpoint γ -ray emission regions of blazars, many methods have been proposed: (i) *variability*: Tavecchio *et al.* 2010 studied the light curves of 3C 454.3 and PKS 1510–089, and found significant short variabilities, which indicates that the dissipation occurs in a very compact region located in the BLR. Dotson *et al.* 2012 proposed that the variability timescale of flares would not change in different bands within the BLR, but should manifest faster variabilities at higher energies within the DT. Applying this method to PKS 1510–089, they analyzed four prominent γ -ray flares detected by *Fermi* in 2009 and concluded that γ -ray emission regions are distributed over an extensive range of locations beyond the BLR (Dotson *et al.* 2015). (ii) *radio core-shift*: Based on radio core-shift measurements, Yan *et al.* 2018 suggested that the distance between the SMBH and the γ -ray emission region is less than 3.5 pc for PKS 1510–089 and less than 0.02 pc for BL Lacertae in the framework of leptonic models. Wu *et al.* 2018 determined the distance to be about ten times the typical size of the BLR for 23 LSPs. Jiang *et al.* 2020 used the time lags to derive the core size and inferred that the γ -ray emission region of PMN J2345–1555 is probably inside the BLR. (iii) *model*: Cao and Wang 2013 reproduced the quasi-simultaneous SEDs of 21 FSRQs using the one-zone leptonic model and inferred that the locations of the γ -ray emission regions are inside the BLR for 5 FSRQs and beyond the BLR for 16 FSRQs. Tan *et al.* 2020 fitted the quasi-simultaneous SEDs of 60 FSRQs with the same model and got similar results. Based on SED fitting, Arsioli and Chang 2018 analysed the electron Lorentz factor and magnetic field strength for 104 LSPs, then found they are consistent with an EC model dominated by the DT. However, SED fitting results are not always reliable due to coupling of physical parameters, underscoring the importance of constraining some of them through direct observations (Yamada *et al.* 2020; Deng *et al.* 2021).

In addition to the above three methods, Georganopoulos,

Meyer, and Fossati 2012 proposed *the seed factor approach* to study if the γ -ray emission region of blazars is located near the BLR or DT. This method provides a convenient approach by utilizing the peak frequencies and luminosities, which can be extracted from the SEDs easily. Harvey, Georganopoulos, and Meyer 2020 further applied this approach to a dataset consisting of 62 FSRQs and demonstrated that the γ -ray emission regions predominantly reside within the DT. This finding was subsequently confirmed by Huang *et al.* 2022, who extended their analysis to a larger sample, including 619 FSRQs.

Recently, the SEDs of blazars in the Fourth *Fermi*-LAT 12-year Source catalog (4FGL-DR3) have been fitted with the quadratic function by Yang *et al.* 2022; Yang *et al.* 2023. We apply *the seed factor approach* to this latest and largest sample of γ -ray LSPs to study their dissipation region positions. Furthermore, considering that blazars are highly variable objects (Dotson *et al.* 2015; Arsioli and Polenta 2018), some flare states of various epochs are collected to investigate alterations in their physical properties. This paper is organized as follows. In Section 2, we present the methods, including *the seed factor approach*, SED fitting, and comprehensive parameter analysis of the γ -ray emission regions. The applications are presented in Section 3. In the end, we draw a conclusion in Section 4. The cosmological parameters $H_0 = 69.6 \text{ km s}^{-1} \text{ Mpc}^{-1}$, $\Omega_0 = 0.29$, and $\Omega_\Lambda = 0.71$ are adopted in this work (Bennett *et al.* 2014).

2. Methods

2.1 Derivation of the Seed Factor

In this work, we adopt *the seed factor approach* to distinguish the location of γ -ray emission region. Following Georganopoulos, Meyer, and Fossati 2012, we have peak energies of synchrotron radiation and EC scattering in the observer's frame,

$$\epsilon_{\text{syn}}^{\text{obs}} = \frac{B}{B_{\text{cr}}} \gamma_b^2 \delta / (1+z), \quad (1)$$

$$\epsilon_{\text{EC}}^{\text{obs}} = \frac{4}{3} \epsilon_{0,\text{ext}} \gamma_b^2 \delta^2 / (1+z), \quad (2)$$

respectively (Coppi and Blandford 1990; Tavecchio, Maraschi, and Ghisellini 1998; Ghisellini and Tavecchio 2008a), where B is the magnetic field strength in units of Gauss; γ_b is the break Lorentz factor of relativistic electrons responsible for the SED peaks; $\epsilon_{0,\text{ext}}$ is the dimensionless energy of ambient soft photons in the AGN frame; $B_{\text{cr}} = m_e^2 c^3 / e \hbar$ is the critical magnetic field strength; $\delta = [\Gamma(1 - \beta \cos \theta_{\text{obs}})]^{-1}$ is the Doppler factor, where Γ is the bulk Lorentz factor, βc is the jet speed and θ_{obs} is the viewing angle. In this paper, by assuming $\theta_{\text{obs}} \lesssim 1/\Gamma$, we have $\delta \approx \Gamma$. It is worth noting that equation (2) is only applicable within the Thomson regime.

Dividing equation (1) by equation (2), we obtain

$$\frac{B}{\delta} = \frac{4 B_{\text{cr}} \epsilon_{0,\text{ext}} \epsilon_{\text{syn}}^{\text{obs}}}{3 \epsilon_{\text{EC}}^{\text{obs}}}. \quad (3)$$

And the peak luminosities of synchrotron radiation and EC scattering in the observer's frame can be written as

$$L_{\text{syn,p}}^{\text{obs}} = \frac{4}{3} \sigma_{\text{T}} c \beta \gamma_b^2 n(\gamma_b) U_B \delta^4, \quad (4)$$

$$L_{\text{EC,p}}^{\text{obs}} = \frac{4}{3} \sigma_{\text{T}} c \beta \gamma_{\text{b}}^2 n(\gamma_{\text{b}}) U_{\text{ext}} \delta^4, \quad (5)$$

respectively (Blumenthal and Gould 1970; Rybicki, Lightman, and Tayler 1981), where σ_{T} is the Thomson cross section; $n(\gamma_{\text{b}})$ is the electron density distribution at γ_{b} ; $U_{\text{B}} = B^2/8\pi$ is the energy density of the magnetic field. Here, the energy density of the ambient photon fields in the comoving frame can be calculated as

$$U_{\text{ext}} = \frac{17}{12} U_{0,\text{ext}} \Gamma^2, \quad (6)$$

where $U_{0,\text{ext}}$ is the energy density in the AGN frame (Ghisellini and Madau 1996; Ghisellini and Tavecchio 2008b).

Take the ratio of equation (4) and equation (5), we then get

$$\frac{B^2}{\delta^2} = \frac{34\pi U_{0,\text{ext}}}{3CD}, \quad (7)$$

where $CD = L_{\text{EC,p}}^{\text{obs}}/L_{\text{syn,p}}^{\text{obs}}$ is the Compton dominance.

Combining equation (3) and equation (7), we ultimately derive the seed factor as

$$SF = \log\left(\frac{\sqrt{U_{0,\text{ext}}}}{\epsilon_{0,\text{ext}}}\right) \approx \log\left(9863 \times \frac{\nu_{\text{syn},13}^{\text{obs}}}{\nu_{\text{EC},22}^{\text{obs}}} \sqrt{CD}\right). \quad (8)$$

Here, $\nu_{\text{syn},13}^{\text{obs}}$ is the peak frequency of synchrotron radiation in units of 10^{13}Hz and $\nu_{\text{EC},22}^{\text{obs}}$ is the peak frequency of EC scattering in units of 10^{22}Hz .

2.2 Characteristic Values of the Seed Factor

As the ambient photon fields, the BLR and DT were discussed in the former *seed factor approach* (Georganopoulos, Meyer, and Fossati 2012; Harvey, Georganopoulos, and Meyer 2020; Huang et al. 2022). In addition, some studies revealed the significance of CMB and starlight (Böttcher, Dermer, and Finke 2008; Potter and Cotter 2013a, 2013b, 2013c). In this work, we comprehensively consider the seed factors of BLR, DT, CMB, and starlight. The accretion disc is out of consideration, because it is not suitable to this method.

To calculate the characteristic seed factor of BLR, the energy density $U_{0,\text{ext}}$ and the dimensionless energy $\epsilon_{0,\text{ext}}$ of the soft photons need to be determined. The typical size of BLR is $R_{\text{BLR}} \approx 1 \times 10^{17} L_{\text{d},45}^{1/2}$ cm, where $L_{\text{d},45}$ is the luminosity of the accretion disc in units of 10^{45}erg s^{-1} (Kaspi et al. 2007; Bentz et al. 2009). The covering factor of BLR (the fractions of the disk luminosity L_{d} reprocessed into the BLR radiation) is $\xi_{\text{BLR}} = 0.1$ (Ghisellini and Tavecchio 2009). We then obtain the energy density $U_{0,\text{BLR}} = \xi_{\text{BLR}} L_{\text{d}}/4\pi R_{\text{BLR}}^2 c = 2.65 \times 10^{-2}\text{erg cm}^{-3}$ within the characteristic distance. The BLR can be regarded as a grey body with peak frequency of $1.5\nu_{\text{Ly}\alpha}$, then the dimensionless photon energy is $\epsilon_{0,\text{BLR}} = 3 \times 10^{-5}$ (Fabrizio Tavecchio and Gabriele Ghisellini 2008). Finally, with a 5% uncertainty, we derive the characteristic seed factor of BLR as $SF_{\text{BLR}} = 3.74 \pm 0.19$.

The typical size of DT is found to be $R_{\text{DT}} \approx 2.5 \times 10^{18} L_{\text{d},45}^{1/2}$ cm (Ghisellini and Tavecchio 2009; Pei et al. 2022). In this work, we set the covering factor of DT as $\xi_{\text{DT}} = 0.5$ (Ghisellini and Tavecchio 2009). Then the energy density of DT within the characteristic distance is $U_{0,\text{DT}} = \xi_{\text{DT}} L_{\text{d}}/4\pi R_{\text{DT}}^2 c = 2.12 \times 10^{-4}\text{erg cm}^{-3}$. In the studies, the DT, which can also be approximated by a grey body, is endowed with three different temperatures, e.g., 80K (Lopez-Rodriguez et al. 2018), 370K (Ghisellini and Tavecchio 2009), 1500K (Almeyda et al. 2017; Lyu and Rieke 2018). Then we obtain three dimensionless photon energies for the DT, which are $\epsilon_{0,\text{DT}}^{80\text{K}} = 5.30 \times 10^{-8}$, $\epsilon_{0,\text{DT}}^{370\text{K}} = 2.45 \times 10^{-7}$, $\epsilon_{0,\text{DT}}^{1500\text{K}} = 9.94 \times 10^{-7}$. Considering the 5% uncertainty, three distinct characteristic seed factors of DT can be described as follows: $SF_{\text{DT}}^{80\text{K}} = 5.44 \pm 0.27$, $SF_{\text{DT}}^{370\text{K}} = 4.77 \pm 0.24$, $SF_{\text{DT}}^{1500\text{K}} = 4.17 \pm 0.21$.

For CMB, the energy density is $U_{\text{CMB}} = 4.02 \times 10^{-13}\text{erg cm}^{-3}$ and the typical temperature is $T_{\text{CMB}} = 2.72\text{K}$ in the observer's frame, respectively (Böttcher, Dermer, and Finke 2008). In this case, the characteristic seed factor of CMB with 5% uncertainty is $SF_{\text{CMB}} = 2.55 \pm 0.13$. The energy density for starlight is $U_{0,\text{SL}} = 8.01 \times 10^{-13}\text{erg cm}^{-3}$ and the typical temperature is $T_{\text{SL}} = 30\text{K}$. Then we get the characteristic seed factor of starlight with 5% uncertainty $SF_{\text{SL}} = 1.65 \pm 0.08$ (H. E. S. S. Collaboration et al. 2017).

When applying the *seed factor approach*, there are several caveats that should be kept in mind. Firstly, the preceding derivation of the seed factor is within the Thomson regime. As a result of $\gamma\epsilon < 1/4$ (Moderski et al. 2005), the corresponding peak frequency of the EC radiation belonging to BLR, DT, CMB and starlight must be less than $1.03 \times 10^{25} [\epsilon_0(1+z)/10^{-6}]^{-1}\text{Hz}$. Since high-energy component of LSP usually peaks around 1 GeV, the EC process associated to BLR occurs in the Klein-Nishina regime, while others are cooling in the Thomson regime. Then the available energy density of BLR could reduce and the actual characteristic seed factor of BLR would be smaller than the above derived one. Secondly, the energy density of the BLR and DT could be smaller at farther site as proposed by Hayashida et al. 2012, i.e.,

$$U_{0,\text{BLR}}(r) = \frac{\xi_{\text{BLR}} L_{\text{d}}}{4\pi R_{\text{BLR}}^2 c [1 + (r/R_{\text{BLR}})^3]}, \quad (9)$$

and

$$U_{0,\text{DT}}(r) = \frac{\xi_{\text{DT}} L_{\text{d}}}{4\pi R_{\text{DT}}^2 c [1 + (r/R_{\text{DT}})^4]}, \quad (10)$$

where r is the distance between the dissipation region and the central black hole, both energy densities of the BLR and DT have been transformed into the AGN frame (see also Figure 1). Then the actual characteristic seed factor could also be smaller if the emission region is beyond the typical distance. Since the above derived characteristic seed factor of DT is the largest one among these four photon fields, the actual seed factor of DT covers that of the others. For example, the actual seed factor of DT could decrease to about 3.5 and equal to the actual seed factor of BLR. Therefore, the above derived seed factor of DT but not of BLR, CMB, or starlight is effective. If

the observed seed factor is approximated to the derived SF_{DT} , it can be ascertained that the DT dominates the soft photon fields.

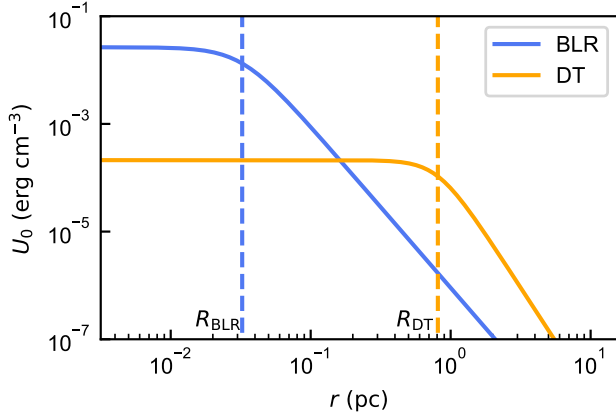


Figure 1. Energy density distribution of the broad line region (BLR) and the dusty torus (DT). $L_d = 1 \times 10^{45} \text{ erg s}^{-1}$ is adopted.

2.3 The Fitting of Spectral Energy Distribution

As shown in equation (8), the observed seed factor can be determined by extracting the peak frequencies and luminosities associated with the two humps. Then we fit each SED by the quadratic and cubic functions, respectively. Namely,

$$\begin{cases} \log(\nu F_\nu) = a_2(\log \nu)^2 + b_2 \log \nu + c_2, \\ \log(\nu F_\nu) = a_3(\log \nu)^3 + b_3(\log \nu)^2 + c_3 \log \nu + d_3. \end{cases} \quad (11)$$

We use two kinds of functions because some SEDs possess high symmetry but others do not, which causes difference on the parameters (R. Xue *et al.* 2016). Markov-chain Monte Carlo (MCMC) analysis is employed since it returns robust uncertainties on the parameters (Speagle 2019). It works by randomly sampling from the posterior distribution, which are derived from the product of prior distribution and likelihood function. We use an uninformative uniform prior distribution because we have little knowledge about the parameters of quadratic and cubic functions in advance. Conservatively, it is expressed by

$$p(m) = \begin{cases} \frac{1}{1000}, & \text{if } m_0 - 500 < m < m_0 + 500 \\ 0, & \text{otherwise} \end{cases} \quad (12)$$

where m denotes the parameters in both quadratic and cubic functions, such as a_2, b_2, \dots . And m_0 is the preprocessed m derived by `numpy.polyfit`^a. The likelihood function is written as (Yamada *et al.* 2020)

$$L = \prod_{i=1}^n \frac{1}{\sqrt{2\pi\sigma_i^2}} \exp\left(-\frac{(\nu F_{\nu,i} - \nu F_\nu(\nu_i))^2}{2\sigma_i^2}\right). \quad (13)$$

a. <https://numpy.org/doc/stable/reference/generated/numpy.polyfit.html>

Here, σ_i is the Gaussian error of data point i and n is the number of data points in each energy hump. The `emcee` Python package^b (version 3.1.2, Foreman-Mackey *et al.* 2013) is utilized to perform the MCMC algorithm. This package employs an affine invariant MCMC ensemble sampler with interdependent chains (Goodman and Weare 2010). While there is no fixed number of samples needed to make the convergence, we evaluate the convergence by inspecting the corner plot of parameters. The autocorrelation time, also the time that the chain "forgets" where it started, range from 35 to 250 in our Python program. Conservatively, we adopt 32 walkers (chains) initialized by the above preprocessed values with a 10^{-10} Gaussian error, run 17000 steps, burn 2000 steps and thin by 25. The results of posterior distribution are presented in Figure 2.

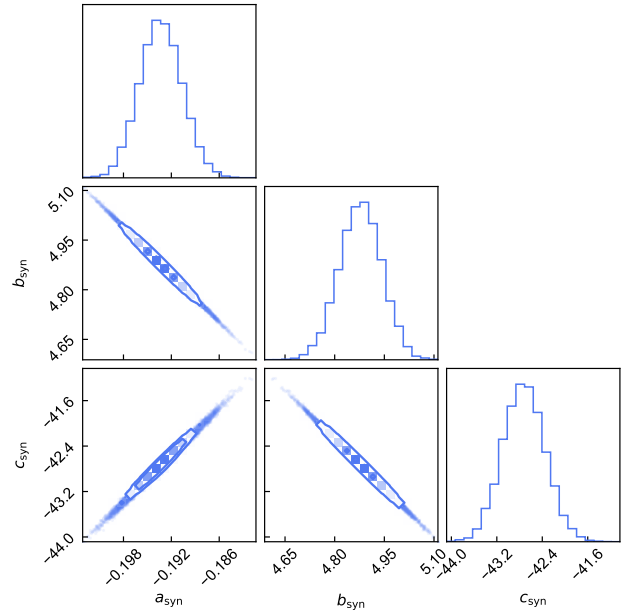


Figure 2. Posterior distribution from the Markov-chain Monte Carlo analysis of OD 166's low-energy (synchrotron) hump with quadratic function. We present only one corner plot here, those of other SEDs are available in machine-readable form.

While fitting the SEDs, we also compare the goodness of the two different function models with modified Akaike Information Criterion (AICc; Akaike 1974; Burnham and Anderson 2002), written as

$$\text{AICc} = -2 \ln(\hat{L}) + 2k + \frac{2k^2 + 2k}{n - k - 1}. \quad (14)$$

In this formula, \hat{L} is the maximum likelihood, which corresponds to the maximum posterior since we used an uniform prior, and k is the number of free parameters. This criterion is chosen because the sample size of data points is small. AICc evaluates the loss of information during the fitting. The smaller

b. <https://emcee.readthedocs.io/en/stable/>

AICc means the better model. Actually, the additional parameters in a model should improve the fitting to the data points, but we should also consider the increase in model complexity which causes overfitting. In this case, the AICc includes a penalty.

2.4 Parameters of the Emission Region

By fitting the SEDs of blazars, the observed peak frequencies and peak luminosities are determined. Then we select the blazars whose seed factors fall within the SF_{DT} . With the gathered information on variability timescales and Doppler factors, we can deduce the other physical parameters of the γ -ray emission region. For blazars, we have such a formula (Tavecchio, Maraschi, and Ghisellini 1998; Nalewajko, Begelman, and Sikora 2014):

$$\frac{L_{\text{syn}}^{\text{obs}}}{U_{\text{B}}} = \frac{L_{\text{EC}}^{\text{obs}}}{U_{\text{ext}}} = \frac{L_{\text{SSC}}^{\text{obs}}}{U_{\text{syn}}}. \quad (15)$$

Here, $L_{\text{syn}}^{\text{obs}}$, $L_{\text{EC}}^{\text{obs}}$, $L_{\text{SSC}}^{\text{obs}}$ are the luminosities of the synchrotron, EC, and SSC radiations, respectively. $L_{\text{syn}}^{\text{obs}}$ and $L_{\text{EC}}^{\text{obs}}$ are determined by the integral of the low-energy and high-energy humps, respectively. For simplicity, we boldly assume that $L_{\text{SSC}}^{\text{obs}} = 10 \times L_{\text{X}}^{\text{obs}}$, where $L_{\text{X}}^{\text{obs}}$ is the maximum luminosity in X-ray band. $U_{\text{syn}} = L_{\text{syn}}^{\text{obs}}/(4\pi R^2 c \delta^4)$ is the energy density of the synchrotron radiation. The radius of the γ -ray emission region in the comoving frame can be estimated as

$$R \approx ct_{\text{var}} \frac{\delta}{1+z}, \quad (16)$$

where t_{var} is the variability timescale.

If we have measured the variability timescale, we can derive the following parameters by combining the above formulas:

$$\begin{cases} \delta = 6.39 \left(\frac{L_{\text{syn}}^{\text{obs}} L_{\text{EC}}^{\text{obs}}}{L_{\text{SSC}}^{\text{obs}} \cdot 10^{45} \text{erg s}^{-1}} \frac{10^{-4} \text{erg cm}^{-3}}{U_{0,\text{ext}}} \right)^{1/8} \left(\frac{t_{\text{var}}}{1d(1+z)} \right)^{-1/4}, \\ R = 1.66 \times 10^{16} \left(\frac{L_{\text{syn}}^{\text{obs}} L_{\text{EC}}^{\text{obs}}}{L_{\text{SSC}}^{\text{obs}} \cdot 10^{45} \text{erg s}^{-1}} \frac{10^{-4} \text{erg cm}^{-3}}{U_{0,\text{ext}}} \right)^{1/8} \left(\frac{t_{\text{var}}}{1d(1+z)} \right)^{3/4}, \\ B = 0.382 \left(\frac{L_{\text{syn}}^{\text{obs} 5}}{L_{\text{EC}}^{\text{obs} 3} L_{\text{SSC}}^{\text{obs}} \cdot 10^{45} \text{erg s}^{-1}} \right)^{1/8} \left(\frac{U_{0,\text{ext}}}{10^{-4} \text{erg cm}^{-3}} \right)^{3/8} \left(\frac{t_{\text{var}}}{1d(1+z)} \right)^{-1/4}. \end{cases} \quad (17)$$

When the Doppler factor is measured, we obtain:

$$\begin{cases} t_{\text{var}} = 1.44 \times 10^4 \left(\frac{L_{\text{syn}}^{\text{obs}} L_{\text{EC}}^{\text{obs}}}{L_{\text{SSC}}^{\text{obs}} \cdot 10^{45} \text{erg s}^{-1}} \frac{10^{-4} \text{erg cm}^{-3}}{U_{0,\text{ext}}} \right)^{1/2} \left(\frac{\delta}{10} \right)^{-4} (1+z), \\ R = 4.33 \times 10^{15} \left(\frac{L_{\text{syn}}^{\text{obs}} L_{\text{EC}}^{\text{obs}}}{L_{\text{SSC}}^{\text{obs}} \cdot 10^{45} \text{erg s}^{-1}} \frac{10^{-4} \text{erg cm}^{-3}}{U_{0,\text{ext}}} \right)^{1/2} \left(\frac{\delta}{10} \right)^{-3}, \\ B = 0.597 \left(\frac{L_{\text{syn}}^{\text{obs}}}{L_{\text{EC}}^{\text{obs}} \cdot 10^{-4} \text{erg cm}^{-3}} \frac{U_{0,\text{ext}}}{10^{-4} \text{erg cm}^{-3}} \right)^{1/2} \frac{\delta}{10}. \end{cases} \quad (18)$$

Besides, γ_{b} can be calculated by (Tavecchio, Maraschi, and Ghisellini 1998)

$$\gamma_{\text{b}} = 5.2 \times 10^{-4} \left(\frac{\nu_{\text{syn}}^{\text{obs}}(1+z)}{B\delta} \right)^{1/2}. \quad (19)$$

2.5 Constraint of the Internal $\gamma\gamma$ -Absorption

To make a comparison with the above derivation of physical parameters, we further make a constraint on δ through $\gamma\gamma$ -absorption (see also Dondi and Ghisellini 1995). Due to the $\gamma\gamma$ annihilation, electron-positron pairs are generated. Applying Delta-approximation, the corresponding optical depth can be calculated as (Foffano et al. 2022):

$$\tau_{\gamma\gamma} = \sigma_{\gamma\gamma} n_{\text{soft}} R, \quad (20)$$

where $n_{\text{soft}} = U_{\text{soft}}/h\nu_{\text{soft}}$ is the number density of the soft photons and $\sigma_{\gamma\gamma} = 1.68 \times 10^{-25} \text{cm}^2$ is the $\gamma\gamma$ -absorption cross section, which is assumed to be a constant when such a condition is fulfilled:

$$\epsilon_{\text{soft}} \epsilon_{\gamma} = 2, \quad (21)$$

where ϵ_{soft} and ϵ_{γ} are the dimensionless energies of the soft photons and γ -ray photons (comoving frame), respectively (Dermer and Menon 2009).

Since the γ -ray is detected, optical depth must be less than 1. In order to solve the optical depth, energy density need to be determined. For internal soft photon fields such as synchrotron and IC radiation, we employ

$$U_{\text{soft}} = \frac{\nu L_{\nu,\text{soft}}^{\text{obs}}}{4\pi R^2 c \delta^4}, \quad (22)$$

where $\nu L_{\nu,\text{soft}}^{\text{obs}} = 4\pi d_{\text{L}}^2 \nu F_{\nu,\text{soft}}^{\text{obs}}$ is the observed luminosity of the soft photons, d_{L} is the luminosity distance, and $\nu F_{\nu,\text{soft}}^{\text{obs}}$ is the observed flux. Then we derive

$$\tau_{\gamma\gamma} = \frac{\sigma_{\gamma\gamma} d_{\text{L}}^2 \nu F_{\nu,\text{soft}}^{\text{obs}}(1+z)}{hc^2 t_{\text{var}} \delta^5 \nu_{\text{soft}}} < 1. \quad (23)$$

Here, ν_{soft} could be derived from equation (21) and expressed by

$$\nu_{\text{soft}} = \frac{2(m_e c^2)^2}{h^2 \nu_{\gamma}}, \quad (24)$$

where $\nu_{\gamma} = \nu_{\gamma}^{\text{obs}}(1+z)/\delta$ is the frequency of γ -ray in the comoving frame. Then we obtain the lower limit of δ :

$$\delta > \left(\frac{h\sigma_{\gamma\gamma} d_{\text{L}}^2 \nu F_{\nu,\text{soft}}^{\text{obs}} \nu_{\gamma}^{\text{obs}}(1+z)^2}{2m_e^2 c^6 t_{\text{var}}} \right)^{1/6}. \quad (25)$$

Not only do internal photon fields constrain the physical parameter, but external photon fields also give an additional constraint on r . The absorption of DT could be omitted according to equation (21), since the corresponding γ -ray ($\nu_{\gamma}^{\text{obs}} = 10^{27}(\nu_{\text{DT}}/10^{13} \text{Hz})^{-1} \text{Hz}$) is beyond detection in our collected SEDs. However, the γ -ray up to $10^{25}(\nu_{\text{BLR}}/10^{15} \text{Hz})^{-1} \text{Hz}$ that is detectable could be absorbed by BLR. Therefore, we inspect the $\gamma\gamma$ -absorption of BLR by unfolding its frequency spectrum. Given that the BLR is a grey body, we have

$$\frac{dU}{d\nu} = \frac{8\pi h\nu^3}{c^3} (e^{h\nu/k_{\text{B}}T} - 1)^{-1}, \quad (26)$$

where $T = h\nu_{\text{BLR}}/3.93k_{\text{B}}$ is the characteristic temperature of BLR and k_{B} is the Boltzmann constant (Ghisellini and Tavecchio 2009). From the combination of equation (9) and (26), we derive the energy density of BLR as a function of both r and ν :

$$U_{\text{BLR}}(r, \nu) = \Gamma^2 U_{0,\text{BLR}}(r) \nu \frac{dU}{d\nu} / \int \frac{dU}{d\nu} d\nu. \quad (27)$$

With the same condition about $\tau < 1$ and lower limit of δ derived from equation (25), we could get the lower limit of r :

$$r > R_{\text{BLR}} \left(\frac{\sigma_{\gamma} \gamma R}{h} \frac{\xi_{\text{BLR}} \Gamma^2 L_{\text{d}}}{3\pi R_{\text{BLR}}^2 c} \frac{dU}{d\nu} \Big|_{\nu=\nu_{\text{soft}}} / \int \frac{dU}{d\nu} d-1 \right)^{1/3}. \quad (28)$$

3. Application

3.1 Low-Synchrotron-Peaked Blazars

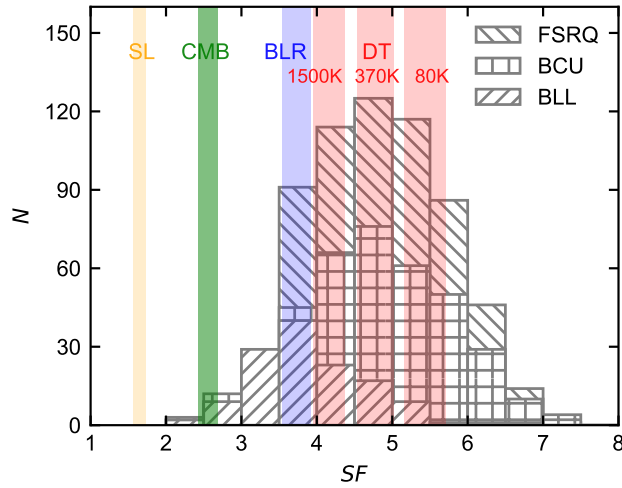


Figure 3. Histogram of observed seed factors. FSRQs, BL Lacs and blazar candidates of uncertain type (BCU) in our sample are distinguished by three kinds of grids. Three red areas represent the scales of characteristic seed factors belonging to the dusty torus (DT) in three different temperatures. Blue, green and yellow areas represent the scales of characteristic seed factors belonging to the broad line region (BLR), cosmic microwave background (CMB) and starlight (SL).

Locating the γ -ray emission region of blazars has been a significant issue in the *Fermi* era. Debates continuously happen because of the limited accuracy of instruments and complicated radiation mechanism of blazars. In this work, we adopted *the seed factor approach* proposed by Georganopoulos, Meyer, and Fossati 2012. Based on the derivation in Section 2.1, some observed quantities need to be determined. We collected a sample of 1138 LSPs with synchrotron peak frequencies and luminosities from Yang et al. 2022, and with IC peak frequencies and luminosities from Yang et al. 2023. There are 630 FSRQs, 132 BL Lacs and 376 blazar candidates of uncertain type (BCUs) in this sample (see also Table 1). The Doppler factors of 383 blazars are also recorded from Lioudakis et al. 2018 for further calculation. Figure 3 displays the histogram of observed seed factors belonging to the LSPs, which is obtained using equation (8). The observed seed factors of FSRQs and

BCUs converge around the areas of DT, which demonstrates that DT dominates the soft photon fields of FSRQs and BCUs. This can be attributed to the strong radiation from DT, which is reproduced by the strong radiation from accretion disc of FSRQs and BCUs (Madejski and Sikora 2016; Huang et al. 2022). The observed seed factors of BL Lacs converge around the area of BLR. This suggests that the soft photons either originate from BLR or from DT, as the actual seed factor of DT could be smaller than the one depicted in Figure 3. The areas of CMB and starlight appear on the left edge of the histogram, indicating that their contributions to the soft photons in the EC process are relatively small. In general, observed seed factors of 552 in 1138 LSPs directly fall into the areas of DT, which locates the γ -ray emission region at 1–10 pc.

This result is consistent with the former analysis using *the seed factor approach*. Harvey, Georganopoulos, and Meyer 2020 calculated the seed factors of 62 FSRQs and found the distribution peaking at a value corresponding to DT. Huang et al. 2022 used a sample of 619 sources and also found the distribution is located at DT. In our work, rather than setting the temperature of DT to 1200K, we considered three different temperatures of DT because it is a relatively thick gas cloud with its inner temperature varying from the outer one (Lyu and Rieke 2018). Figure 3 shows 370K dominates the distribution of observed seed factors, indicating most γ -ray emission regions are located inside the DT.

3.2 LSPs Dominated by the Dusty Torus

Although our result suggests that DT dominates the soft photon fields of LSPs, previous study demonstrated that blazars might have various γ -ray emission regions in different flare epochs (Dotson et al. 2015). We investigated this property by collecting some historical flare states. LSPs whose observed seed factors directly fall into the red areas in Figure 3 (i.e., LSPs dominated by the DT) were selected, since only their soft photon fields had been determined effectively. The SEDs that we collected fulfilled these conditions: Possessing multi-wavelength quasi-simultaneous data except for the radio band. The observation times of each band intersect within two months. In total, we collected 23 SEDs. The related references are given in Table 2. These SEDs were fitted by both quadratic and cubic functions using the MCMC method (see also Figures 7 & 8). Then we extracted the peak frequencies and luminosities of two humps, and calculated the observed seed factors. The results are displayed as scatterplots in Figure 4. The distributions of data scatters vary under two different function fits. This demonstrates that the values of seed factors are significantly influenced by the choice of the function. On the other hand, both fitting results of two different functions show that some scatters, i.e., 7 scatters of quadratic function and 9 scatters of cubic function, move outside DT areas. Although the actual seed factor of DT could be smaller and cover them, they have already moved to the areas of BLR or CMB. This indicates that the location of γ -ray emission region changed in historical flare states, and the soft photon fields could transition from DT to BLR and CMB.

Table 1. Observed quantities and seed factors of 1138 low-synchrotron-peaked blazars.

Fermi Name (1)	Classification (2)	z (3)	$\log \nu_{\text{syn}}^{\text{obs}}$ (4)	$\log L_{\text{syn}}^{\text{obs}}$ (5)	$\log \nu_{\text{IC}}^{\text{obs}}$ (6)	$\log L_{\text{IC}}^{\text{obs}}$ (7)	SF (8)	δ (9)
4FGL J0001.5+2113	FSRQ	1.106	13.2	46.17	20.6	47.21	6.10	
4FGL J0003.3-1928	BCU	2.000	13.3	46.21	22.5	46.42	3.90	
4FGL J0003.9-1149	BLL	0.860	13.2	45.9	23.1	45.28	2.81	
4FGL J0004.3+4614	FSRQ	1.810	13.1	45.93	21.2	46.84	5.35	7.75
4FGL J0004.4-4737	FSRQ	0.880	13	45.96	21.7	45.89	4.30	
...

NOTE: Column (1) gives the Fermi name. Column (2) represents the spectral classification. Column (3) gives the redshift. Column (4) and (5) are the synchrotron peak frequencies and luminosities from Yang et al. 2022, respectively. Column (6) and (7) are the IC peak frequencies and luminosities from Yang et al. 2023, respectively. Column (8) gives the observed seed factors. Column (9) gives the Doppler factors of 383 blazars from Lioudakis et al. 2018. We present only 5 items here, full table is available in machine-readable form.

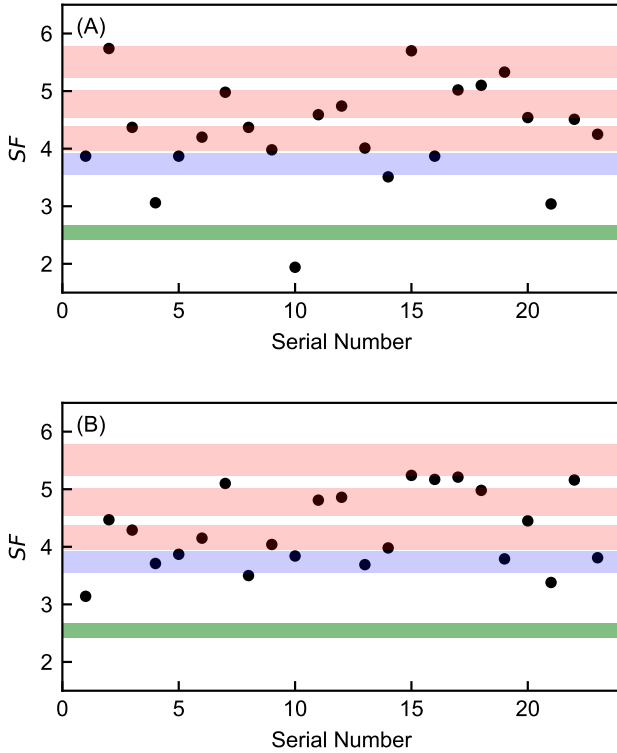


Figure 4. Scatterplots of observed seed factors belonging to low-synchrotron-peaked blazars dominated by the dusty torus. These data correspond to the first 23 flare states in Table 2, ordered from top to bottom. The upper and lower panels are derived from SEDs fitted by quadratic and cubic functions, respectively. Red, blue and green areas depict the characteristic seed factors of dusty torus, broad line region and cosmic microwave background, respectively.

3.3 Four Typical Low-Synchrotron-Peaked Blazars

In order to further verify the alteration of γ -ray emission region in different flare epochs, we collected SEDs of four typical LSPs, including 7 SEDs of CTA 102, 7 SEDs of 3C 279, 3 SEDs of TXS 0506+056 and 5 SEDs of OJ 287. The references of these SEDs are presented in Table 2. These SEDs fulfilled the same conditions as above. Similarly, we fitted these SEDs with both quadratic and cubic functions (see also Figures 9 to 12), extracted the peak frequencies and luminosities, and created the scatterplots of observed seed factors (see also Figure 5). The scatter distributions still vary significantly under two different function fits. Figure 5 also shows that the observed seed factors of the same LSPs are variable in different flare states. Some scatters are positioned in red areas, while others are not, indicating multiple locations of γ -ray emission regions in the same blazar. Some previous studies also support our results. Patiño-Álvarez et al. 2018 collected multi-wavelength light curves for 3C 279 over 6 years and divided them into three flaring periods. They analyzed the time delays and γ -ray spectral index, then found that the dominant radiation mechanism and γ -ray emission regions varied in different periods. Similar to the above LSPs, Deng and Jiang 2023 located the γ -ray emission region of OT 081 at the edge of BLR during the 2016 multiwavelength flare and at about 1-10 pc away from the black hole during the 2009-2012 orphan X-ray flare. Given to the variability of blazars, broadtime analysis has become a typical approach of *Fermi*-LAT to reduce the impact of some short-lived flares (Arsioli and Polenta 2018).

On September 22 2017, the IceCube Observatory detected a ~ 290 TeV neutrino from the direction of TXS 0506+056 (IceCube Collaboration et al. 2018; Padovani et al. 2018). The neutrino was produced in the photopion process, in which the $\Delta^+(1232)$ resonance contributes the main cross section. Using Delta-approximation, we could derive the external soft photon energy in the AGN frame,

$$E_{0,\text{soft}} \simeq \frac{50\text{eV}}{1+z} \left(\frac{\delta}{\Gamma} \right) \left(\frac{290\text{TeV}}{E_{\nu}^{\text{obs}}} \right). \quad (29)$$

It shows that the dissipation region was in the BLR. This neutrino event was closely followed by two very high energy

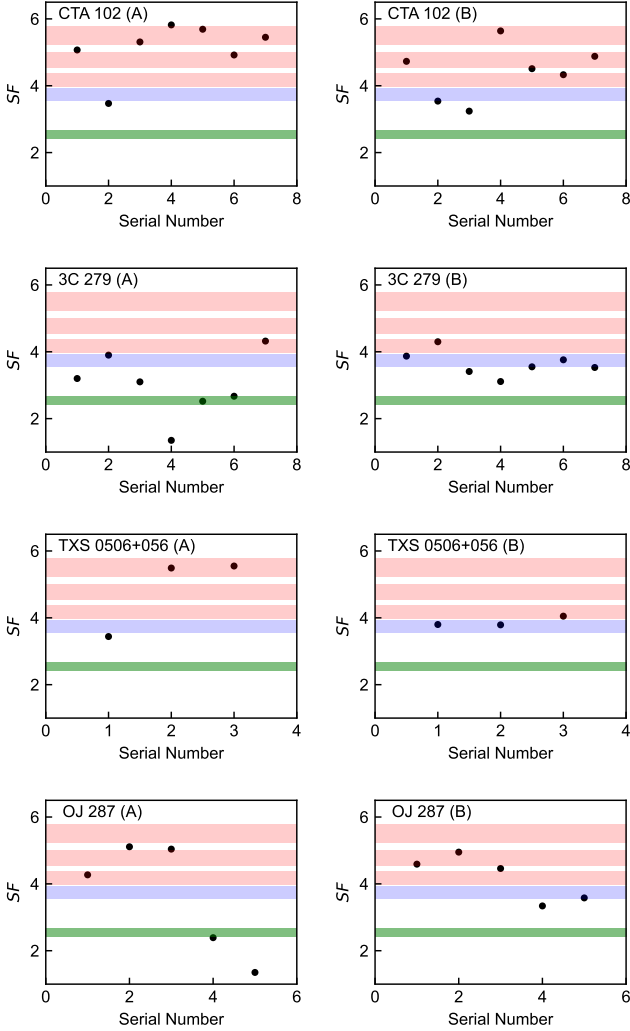


Figure 5. From top to bottom, the scatterplots represent the observed seed factor distributions of historical states for CTA 102, 3C 279, TXS 0506+056, and OJ 287, respectively. The left and right panels are derived from SEDs fitted by quadratic and cubic functions, respectively. Red, blue and green areas depict the characteristic seed factors of dusty torus, broad line region and cosmic microwave background, respectively.

γ -ray flares of TXS 0506+056 (Ansoldi et al. 2018; Narek Sahakyan 2018). These flares were denoted as Flare 2 and Flare 3 in Figure 11. The seed factors are presented in Figure 5, corresponding to serial number 2 and 3. Result of quadratic function depicts that the dissipation region was in the DT, contradicting the above calculation. But that of cubic function approximately supports the BLR. This manifests the difference between two functions and possible superiority of cubic function.

3.4 Model Comparison and Parameter Analysis

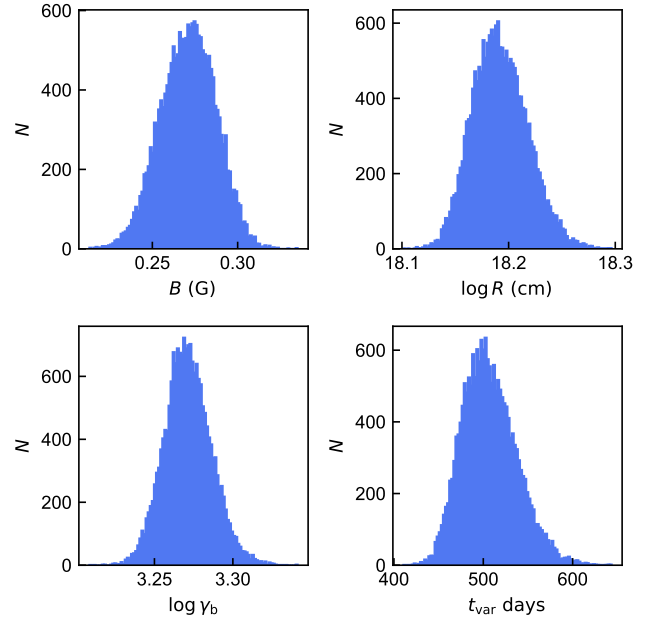


Figure 6. Parameter distribution of OD 166 when Doppler factor is known. Possible value counts of each parameter is 19200 ($=32 \times (17000-2000)/25$) in total. The number of bins is 100. We present only one sample here, others are available in machine-readable form.

We found that different authors adopted various functions to fit the SEDs. Abdo, Ackermann, Agudo, et al. 2010b employed the cubic function, while Chen 2014; Yang et al. 2022; Yang et al. 2023 used a simpler quadratic function. R. Xue et al. 2016 fitted the Synchrotron hump with both functions and found the derived Synchrotron luminosity with cubic function is lower. In this work, we tried both of the two to further illuminate the difference. The AICc of each hump derived from two functions are presented on the figures in Appendix. For the low-energy humps, 33 (45 in total, one is null because $n = k + 1$) AICc of cubic function are smaller. As for high-energy humps, 35 (45 in total) AICc of cubic function are smaller. This demonstrates a dominance of cubic function over quadratic function both in two kinds of humps. We found that the humps with perfect symmetry could be fitted well (i.e., smaller AICc) with quadratic function, such as low-energy humps in PKS 2123-463, OJ 287 Flare 3, OJ 287 Flare 4, etc., and high-energy humps in PKS 0208-512 Flare 1, PKS 0402-362 Flare 2, PKS 0420+022, etc. The asymmetrical SEDs,

which take the most part of our samples, could be explained well with cubic function. On the other hand, we found some quadratic function curves deviate badly from the GeV data points, such as PKS 0208–512 Flare 2, TXS 0506+056 Flare 1, and NARO 512. It is worth noting that GeV data is rarer than other wavebands' in practical, given that the γ -ray telescopes are relatively scarce. Thus the goodness of fit of data points in GeV band has superiority. For 3C 279 Flare 4 and CTA 102 Flare 3, the quadratic function curves in high-energy hump even continually increase, which breaks the physical reality. Therefore, we recommend the cubic function to fit the SEDs.

However, cubic function is not suitable to all the SEDs, such as high-energy humps in TXS 0536+145 and CTA 102 Flare 3 (see Appendix). The hard γ -ray spectra and lack of higher-energy data make it difficult to form a full peak. We also noticed that the conventional one-zone leptonic or hadronic model could hardly explain the SEDs of bright TeV blazars, which results in extreme values (Abdo et al. 2011; Cerruti et al. 2015; Li et al. 2022). In this case, some models of inhomogeneous jet were constructed, such as spine-layer model (Ghisellini, Tavecchio, and Chiaberge 2005; F. Tavecchio and G. Ghisellini 2014), two-zone leptonic model (Shukla et al. 2015) and two-zone leptohadronic model (Aguilar-Ruiz et al. 2022).

Besides collecting the quasi-simultaneous data and fitting the SEDs, we collected the corresponding Doppler factor from Liodakis et al. 2018 or observed variability timescales from the original work, and obtained the distribution of some related parameters using formulas in Section 2.4. For example, Figure 6 presents the derived parameter distribution of OD 166 when the corresponding Doppler factor from Liodakis et al. 2018 is known. There are 19200 possible values for each parameter from the MCMC fitting. The 16–50–84 percentile rule is employed to characterize parameter uncertainty. The detailed results of parameter analysis are listed in Table 2. The average value for variability timescale, Doppler factor, magnetic field strength, radius of emission region, and break Lorentz factor of electrons are 36.58 days, 23.40, 0.674 G, 3.540×10^{16} cm, and 845.28, respectively. Table 2 shows that the physical parameters of a specific blazar changed in different flaring epochs. Feng et al. 2022 reproduced the SEDs of various flares belonging to 3C 454.3 under a one-zone leptonic scenario and found similar variations in physical parameters. Interestingly, Table 2 demonstrates that parameters under two different function fits are analogous, which is unlike the scatterplots. This could be attributed to the effect of symmetry in two humps. It causes more influences in peak frequencies which are mainly used to calculate the observed seed factors, but less in the integral of two humps which are used to calculate the other parameters. We also constrained the Doppler factors and r for the collected LSPs whose observed timescales are known. Table 2 depicts that all the former derived Doppler factors are consistent with their corresponding lower limit. We noticed that some lower limits of r equal to 0. Because the results of derivation in Section 2.5 are negative numbers, but r must be non-negative numbers in real world. This indicates that the constraint of internal $\gamma\gamma$ -absorption on r is relatively weak.

4. Conclusions

In this work, we calculated the observed seed factors of 1138 LSPs and the characteristic seed factors of four external photon fields, then plotted the histogram distribution to locate the γ -ray emission region. SEDs related to historical flare states were collected to investigate the variable locations. These SEDs were fitted by both quadratic and cubic functions using the MCMC method. Furthermore, we derived some parameters of emission region and employed a constraint of internal $\gamma\gamma$ -absorption to verify the derivation. Our main results are as follows:

1. We find that DT dominates the soft photon fields of LSPs and γ -ray emission regions of LSPs are mainly located at 1–10 pc. Histogram shows that the corresponding distribution of BL Lacs peaks at the area of BLR, but this area could also be covered by the actual value of DT. CMB and starlight make little contribution to the γ -ray emission of LSPs.
2. The locations of γ -ray emission region of LSPs are variable in different flare epochs. Most γ -ray emission regions are within the DT, but the soft photon fields could also transition to BLR and CMB.
3. The cubic function is better than the quadratic function to fit the SEDs of blazars. We find that some high-energy humps of blazars cannot be fitted well by quadratic function due to the symmetry of the SEDs.

Acknowledgement

We thank the anonymous referee for valuable comments and constructive suggestions. This work is supported by the National Natural Science Foundation of China (NSFC) under Grant No. 12203043, 12203024 and 12263009.

5. Data Availability

The data derived in this paper are available on Zenodo with a DOI 10.5281/zenodo.11119117^c.

References

- Abdo, A. A., M. Ackermann, I. Agudo, M. Ajello, H. D. Aller, M. F. Aller, E. Angelakis, et al. 2010a. The Spectral Energy Distribution of Fermi Bright Blazars. *ApJ* 716, no. 1 (June): 30–70. <https://doi.org/10.1088/0004-637X/716/1/30>. arXiv: 0912.2040 [astro-ph.CO].
- . 2010b. The Spectral Energy Distribution of Fermi Bright Blazars. *ApJ* 716, no. 1 (June): 30–70. <https://doi.org/10.1088/0004-637X/716/1/30>. arXiv: 0912.2040 [astro-ph.CO].
- Abdo, A. A., M. Ackermann, M. Ajello, A. Allafort, E. Antolini, W. B. Atwood, M. Axelsson, L. Baldini, J. Ballet, G. Barbiellini, D. Bastieri, B. M. Baughman, K. Bechtol, R. Bellazzini, F. Belli, et al. 2010. Fermi Large Area Telescope First Source Catalog. *ApJS* 188, no. 2 (June): 405–436. <https://doi.org/10.1088/0067-0049/188/2/405>. arXiv: 1002.2280 [astro-ph.HE].

c. <https://zenodo.org/records/11119118>

Table 2. Results of parameter analysis.

Fermi Name	Source Name	Time	t_{var}	δ	B	$\log R$	$\log \gamma_b$	δ_{low}	r_{low}	Ref
(1)	(2)	(3)	(days)	(5)	(G)	(cm)	(8)	(9)	(pc)	(11)
4FGL J0242.3+1102*	OD 166	2013.04.18-2013.07.27	504.1 $^{+32.78}_{-27.82}$ 627.67 $^{+15.68}_{-15.72}$	4.37	0.272 $^{+0.015}_{-0.017}$ 0.270 $^{+0.007}_{-0.007}$	18.191 $^{+0.027}_{-0.025}$ 18.286 $^{+0.011}_{-0.011}$	3.271 $^{+0.015}_{-0.014}$ 3.006 $^{+0.014}_{-0.014}$			1
4FGL J1354.8-1041*	PKS 1352-104	2008.08.11-2008.09.11	7.45 $^{+0.20}_{-0.20}$ 6.84 $^{+0.23}_{-0.22}$	6.85	0.229 $^{+0.006}_{-0.006}$ 0.283 $^{+0.009}_{-0.009}$	16.997 $^{+0.012}_{-0.012}$ 16.959 $^{+0.014}_{-0.014}$	3.657 $^{+0.027}_{-0.027}$ 3.280 $^{+0.044}_{-0.043}$			2
4FGL J1549.5+0236*	PKS 1546+027	2010.01.18-2010.03.18	3.80 $^{+0.09}_{-0.09}$ 3.39 $^{+0.09}_{-0.08}$	10.75	0.221 $^{+0.005}_{-0.006}$ 0.247 $^{+0.006}_{-0.006}$	16.874 $^{+0.011}_{-0.011}$ 16.825 $^{+0.011}_{-0.010}$	3.021 $^{+0.010}_{-0.010}$ 2.991 $^{+0.012}_{-0.011}$			3
4FGL J1635.2+3808*	4C +38.41	2010.02.07-2010.04.07	0.58 $^{+0.02}_{-0.02}$ 0.65 $^{+0.05}_{-0.04}$	26.96	1.274 $^{+0.057}_{-0.050}$ 1.222 $^{+0.077}_{-0.080}$	16.160 $^{+0.017}_{-0.019}$ 16.208 $^{+0.029}_{-0.027}$	2.376 $^{+0.010}_{-0.011}$ 2.412 $^{+0.016}_{-0.014}$			3
4FGL J1640.4+3945*	NRAO 512	2010.07.07-2010.09.07	0.31 $^{+0.02}_{-0.02}$ 0.32 $^{+0.02}_{-0.01}$	31.29	0.960 $^{+0.070}_{-0.059}$ 0.974 $^{+0.048}_{-0.044}$	15.973 $^{+0.029}_{-0.032}$ 15.980 $^{+0.020}_{-0.021}$	2.518 $^{+0.017}_{-0.018}$ 2.515 $^{+0.012}_{-0.012}$			3
4FGL J0438.4-1254*	PKS 0436-129	2010.06.01-2010.08.01	0.05 $^{+0.00}_{-0.00}$ 0.04 $^{+0.00}_{-0.00}$	46.93	0.549 $^{+0.017}_{-0.018}$ 0.623 $^{+0.030}_{-0.032}$	15.423 $^{+0.014}_{-0.014}$ 15.335 $^{+0.023}_{-0.021}$	2.579 $^{+0.017}_{-0.016}$ 2.494 $^{+0.020}_{-0.020}$			3
4FGL J2110.2-1021c*	PKS 2107-105	unknown	337.97 $^{+14.27}_{-13.39}$ 359.10 $^{+13.19}_{-13.47}$	4.03	0.143 $^{+0.006}_{-0.006}$ 0.142 $^{+0.006}_{-0.006}$	18.004 $^{+0.018}_{-0.018}$ 18.030 $^{+0.016}_{-0.016}$	3.482 $^{+0.024}_{-0.022}$ 3.478 $^{+0.025}_{-0.026}$			4
4FGL J1345.5+4453*	B3 1343+451	2013.07.27	0.10 $^{+0.00}_{-0.00}$ 0.10 $^{+0.00}_{-0.00}$	45.61	0.647 $^{+0.014}_{-0.013}$ 0.628 $^{+0.014}_{-0.014}$	15.542 $^{+0.009}_{-0.009}$ 15.517 $^{+0.009}_{-0.009}$	2.624 $^{+0.010}_{-0.011}$ 2.538 $^{+0.017}_{-0.018}$			1
4FGL J0210.7-5101	PKS 0208-512	2016.10.20-2016.11.10	8.45	10.67 $^{+0.19}_{-0.22}$	0.414 $^{+0.026}_{-0.021}$	17.066 $^{+0.008}_{-0.009}$	2.993 $^{+0.008}_{-0.013}$	3.06	0	5
		2019.12.14-2019.12.25	5.21	10.81 $^{+0.35}_{-0.25}$ 12.74 $^{+0.07}_{-0.06}$	0.398 $^{+0.030}_{-0.036}$ 0.197 $^{+0.003}_{-0.003}$	17.072 $^{+0.014}_{-0.010}$ 16.934 $^{+0.002}_{-0.002}$	2.990 $^{+0.021}_{-0.016}$ 3.160 $^{+0.002}_{-0.009}$	3.16	0	5
				12.26 $^{+0.07}_{-0.07}$	0.220 $^{+0.004}_{-0.004}$	16.917 $^{+0.003}_{-0.002}$	3.130 $^{+0.011}_{-0.010}$	4.75	0.069	
4FGL J0403.9-3605	PKS 0402-362	2010.01.20-2010.03.01	2.20	17.92 $^{+0.08}_{-0.08}$	0.480 $^{+0.008}_{-0.008}$	16.625 $^{+0.002}_{-0.002}$	2.771 $^{+0.008}_{-0.007}$	7.23	0.043	6
				17.79 $^{+0.08}_{-0.08}$	0.435 $^{+0.008}_{-0.007}$	16.622 $^{+0.002}_{-0.002}$	2.735 $^{+0.012}_{-0.012}$	7.23	0.043	
		2010.03.01-2010.03.21	2.20	18.58 $^{+0.11}_{-0.11}$	0.455 $^{+0.010}_{-0.010}$	16.640 $^{+0.003}_{-0.002}$	2.948 $^{+0.012}_{-0.012}$	7.34	0.059	6
				18.63 $^{+0.11}_{-0.11}$	0.460 $^{+0.010}_{-0.010}$	16.641 $^{+0.002}_{-0.003}$	2.804 $^{+0.021}_{-0.020}$	7.59	0.06	
		2011.09.20-2011.10.04	2.75	23.22 $^{+0.11}_{-0.11}$	0.371 $^{+0.008}_{-0.008}$	16.834 $^{+0.002}_{-0.002}$	2.765 $^{+0.011}_{-0.010}$	5.70	0.044	6
				23.17 $^{+0.10}_{-0.10}$	0.384 $^{+0.007}_{-0.006}$	16.642 $^{+0.003}_{-0.003}$	2.804 $^{+0.021}_{-0.020}$	5.88	0.045	
		2014.07.31-2014.08.17	3.57	19.64 $^{+0.08}_{-0.08}$	0.562 $^{+0.009}_{-0.009}$	16.875 $^{+0.002}_{-0.002}$	2.756 $^{+0.011}_{-0.011}$	5.01	0.023	6
				19.61 $^{+0.09}_{-0.09}$	0.558 $^{+0.009}_{-0.010}$	16.873 $^{+0.002}_{-0.002}$	2.688 $^{+0.010}_{-0.011}$	5.01	0.023	
4FGL J0530.9+1332	PKS 0528+134	2009.09.08	0.94	27.06 $^{+0.27}_{-0.28}$	0.648 $^{+0.025}_{-0.024}$	16.335 $^{+0.004}_{-0.005}$	2.976 $^{+0.031}_{-0.029}$	6.48	0.039	7
				28.21 $^{+0.65}_{-0.62}$	1.290 $^{+0.153}_{-0.136}$	16.353 $^{+0.010}_{-0.010}$	2.829 $^{+0.029}_{-0.029}$	6.73	0.041	
4FGL J0539.6+1432	TXS 0536+145	2012.03.04-2012.04.04	1.00	30.33 $^{+0.46}_{-0.45}$	0.907 $^{+0.054}_{-0.054}$	16.328 $^{+0.007}_{-0.006}$	2.928 $^{+0.035}_{-0.033}$	7.71	0.061	8
				29.90 $^{+0.62}_{-0.59}$	0.721 $^{+0.049}_{-0.045}$	16.322 $^{+0.009}_{-0.009}$	3.051 $^{+0.036}_{-0.036}$	9.45	0.071	
4FGL J2253.9+1609	3C 454.3	2011.01.27-2011.02.08	0.78	24.39 $^{+0.11}_{-0.11}$	0.758 $^{+0.015}_{-0.015}$	16.425 $^{+0.002}_{-0.002}$	2.715 $^{+0.007}_{-0.007}$	7.47	0	9
				25.27 $^{+0.22}_{-0.21}$	0.933 $^{+0.038}_{-0.036}$	16.440 $^{+0.004}_{-0.004}$	2.739 $^{+0.008}_{-0.007}$	7.85	0	
		2010.11.11-2010.12.06	0.78	26.98 $^{+0.14}_{-0.14}$	0.387 $^{+0.009}_{-0.009}$	16.468 $^{+0.002}_{-0.002}$	3.007 $^{+0.018}_{-0.016}$	8.32	0.066	9
				27.02 $^{+0.13}_{-0.13}$	0.386 $^{+0.009}_{-0.009}$	16.469 $^{+0.002}_{-0.002}$	3.037 $^{+0.018}_{-0.018}$	7.77	0.063	
		2011.05.19-2012.09.30	0.56	19.20 $^{+0.14}_{-0.14}$	0.698 $^{+0.017}_{-0.017}$	16.172 $^{+0.003}_{-0.003}$	2.809 $^{+0.008}_{-0.008}$	5.21	0	10
				20.15 $^{+0.14}_{-0.14}$	0.711 $^{+0.016}_{-0.016}$	16.193 $^{+0.003}_{-0.003}$	2.583 $^{+0.015}_{-0.015}$	5.38	0	
4FGL J2329.3-4955	PKS 2326-502	2010.07.31-2010.09.29	0.53	17.05 $^{+0.23}_{-0.24}$	0.173 $^{+0.012}_{-0.012}$	16.190 $^{+0.006}_{-0.006}$	2.995 $^{+0.025}_{-0.024}$	2.86	0	11
				20.03 $^{+1.16}_{-1.18}$	0.456 $^{+0.148}_{-0.119}$	16.260 $^{+0.024}_{-0.026}$	2.945 $^{+0.050}_{-0.058}$	3.87	0	
		2012.06.25-2012.07.05	1.50	18.39 $^{+0.41}_{-0.37}$	0.220 $^{+0.024}_{-0.020}$	16.674 $^{+0.010}_{-0.009}$	2.934 $^{+0.026}_{-0.027}$	1.88	0	11
				20.10 $^{+0.38}_{-0.33}$	0.437 $^{+0.024}_{-0.025}$	16.713 $^{+0.008}_{-0.007}$	3.014 $^{+0.017}_{-0.016}$	1.98	0	
4FGL J2126.3-4605	PKS 2123-463	2011.12.10-2011.12.19	1.97	19.57 $^{+0.26}_{-0.26}$	0.280 $^{+0.013}_{-0.012}$	16.572 $^{+0.006}_{-0.006}$	3.456 $^{+0.057}_{-0.051}$	4.20	0	12
				19.82 $^{+0.30}_{-0.28}$	0.269 $^{+0.014}_{-0.013}$	16.578 $^{+0.007}_{-0.006}$	3.467 $^{+0.062}_{-0.062}$	4.35	0	
4FGL J0108.6+0134	4C +01.02	2015.11.23-2015.12.15	0.66	31.85 $^{+0.11}_{-0.11}$	0.271 $^{+0.003}_{-0.003}$	16.245 $^{+0.002}_{-0.002}$	2.695 $^{+0.003}_{-0.003}$	6.84	0.051	13
				33.00 $^{+0.12}_{-0.12}$	0.343 $^{+0.004}_{-0.004}$	16.260 $^{+0.006}_{-0.002}$	2.803 $^{+0.001}_{-0.003}$	8.43	0.061	

Table 2. -continued.

Fermi Name	Source Name	Time	t_{var}	δ	B	$\log R$	$\log \Upsilon_b$	δ_{low}	r_{low}	Ref
(1)	(2)	(3)	(4)	(5)	(6)	(7)	(8)	(9)	(10)	(11)
			(days)		(G)	(cm)			(pc)	
4FGL J1256.1-0547	3C 279	2014.04.03-2014.04.07	0.09	$41.50^{+0.22}_{-0.23}$	$1.354^{+0.030}_{-0.030}$	$15.790^{+0.002}_{-0.002}$	$2.445^{+0.013}_{-0.014}$	7.96	0.005	14
				$42.00^{+0.24}_{-0.24}$	$1.181^{+0.030}_{-0.029}$	$15.804^{+0.002}_{-0.002}$	$2.422^{+0.002}_{-0.012}$	7.96	0.005	
		2012.04.03	0.08	$44.36^{+0.30}_{-0.29}$	$0.562^{+0.012}_{-0.013}$	$15.795^{+0.003}_{-0.002}$	$2.695^{+0.013}_{-0.013}$	8.79	0	15
				$43.58^{+0.27}_{-0.27}$	$0.593^{+0.014}_{-0.014}$	$15.787^{+0.003}_{-0.003}$	$2.684^{+0.002}_{-0.011}$	9.63	0	
		2011.02.08-2011.04.12	3.49	$13.49^{+0.12}_{-0.13}$	$1.096^{+0.044}_{-0.043}$	$16.900^{+0.009}_{-0.009}$	$2.526^{+0.028}_{-0.028}$	2.87	0	16
				$14.33^{+0.35}_{-0.34}$	$1.514^{+0.181}_{-0.167}$	$16.926^{+0.010}_{-0.011}$	$2.530^{+0.010}_{-0.031}$	2.87	0	
		2011.06.01-2011.06.08	3.49	$15.01^{+0.46}_{-0.39}$	$0.456^{+0.038}_{-0.039}$	$16.945^{+0.012}_{-0.013}$	$3.389^{+0.020}_{-0.021}$	3.30	0	16
				$14.88^{+0.15}_{-0.16}$	$0.931^{+0.034}_{-0.032}$	$16.942^{+0.004}_{-0.005}$	$2.523^{+0.004}_{-0.009}$	3.30	0	
		2014.03.25-2014.04.02	11.61	$11.73^{+0.06}_{-0.06}$	$0.358^{+0.007}_{-0.006}$	$17.361^{+0.002}_{-0.002}$	$3.046^{+0.009}_{-0.010}$	2.76	0	16
				$11.23^{+0.05}_{-0.05}$	$0.402^{+0.007}_{-0.007}$	$17.342^{+0.002}_{-0.002}$	$3.011^{+0.002}_{-0.008}$	3.07	0	
		2015.06.16	3.17	$18.02^{+0.13}_{-0.10}$	$0.106^{+0.003}_{-0.003}$	$16.973^{+0.003}_{-0.003}$	$3.266^{+0.016}_{-0.015}$	4.31	0	16
				$16.39^{+0.11}_{-0.10}$	$0.131^{+0.003}_{-0.003}$	$16.943^{+0.003}_{-0.003}$	$3.244^{+0.003}_{-0.015}$	4.44	0	
		2010.01.14-2010.06.28	2.89	$12.24^{+0.08}_{-0.08}$	$0.745^{+0.022}_{-0.021}$	$16.776^{+0.004}_{-0.004}$	$2.552^{+0.011}_{-0.011}$	3.48	0	10
				$12.75^{+0.09}_{-0.10}$	$0.708^{+0.025}_{-0.022}$	$16.794^{+0.003}_{-0.003}$	$2.416^{+0.003}_{-0.007}$	3.48	0	
4FGL J2232+1143	CTA 102	2016.12.23	0.56	$27.80^{+0.12}_{-0.12}$	$0.771^{+0.013}_{-0.013}$	$16.298^{+0.002}_{-0.002}$	$2.940^{+0.002}_{-0.009}$	6.97	0	17
				$27.25^{+0.32}_{-0.25}$	$0.702^{+0.025}_{-0.025}$	$16.289^{+0.005}_{-0.005}$	$2.962^{+0.013}_{-0.013}$	6.97	0	
		2012.09.18-2012.10.03	3.93	$21.20^{+0.15}_{-0.15}$	$0.225^{+0.005}_{-0.005}$	$17.022^{+0.003}_{-0.003}$	$3.247^{+0.003}_{-0.009}$	6.06	0.105	18
				$20.83^{+0.27}_{-0.24}$	$0.224^{+0.008}_{-0.009}$	$17.018^{+0.005}_{-0.006}$	$3.247^{+0.011}_{-0.011}$	5.98	0.104	
		2017.04.19	0.17	$68.81^{+1.79}_{-1.81}$	$0.170^{+0.013}_{-0.014}$	$16.172^{+0.012}_{-0.011}$	$3.135^{+0.014}_{-0.014}$	11.33	0	19
				$57.05^{+2.91}_{-2.53}$	$0.243^{+0.036}_{-0.035}$	$16.091^{+0.020}_{-0.021}$	$3.117^{+0.029}_{-0.027}$	11.70	0	
		2017.01.08	0.05	$69.69^{+0.25}_{-0.25}$	$1.487^{+0.027}_{-0.028}$	$15.601^{+0.002}_{-0.002}$	$3.061^{+0.006}_{-0.006}$	16.60	0.040	20
				$76.81^{+0.31}_{-0.30}$	$1.964^{+0.030}_{-0.030}$	$15.643^{+0.002}_{-0.002}$	$3.120^{+0.006}_{-0.006}$	15.95	0.039	
		2016.12.30	0.50	$38.33^{+0.18}_{-0.18}$	$0.573^{+0.012}_{-0.012}$	$16.387^{+0.002}_{-0.002}$	$3.371^{+0.009}_{-0.009}$	9.96	0.072	21
				$31.29^{+0.67}_{-0.66}$	$0.217^{+0.024}_{-0.022}$	$16.290^{+0.009}_{-0.009}$	$3.073^{+0.065}_{-0.066}$	10.45	0.075	
		2016.12.26-2016.12.31	0.21	$49.42^{+0.17}_{-0.17}$	$1.421^{+0.021}_{-0.022}$	$16.121^{+0.001}_{-0.002}$	$3.073^{+0.001}_{-0.006}$	16.15	0.064	22
				$52.23^{+0.38}_{-0.37}$	$1.954^{+0.069}_{-0.065}$	$16.150^{+0.003}_{-0.003}$	$2.663^{+0.026}_{-0.027}$	13.39	0.555	
		2011.09.04-2011.10.18	2.49	$14.77^{+0.11}_{-0.11}$	$0.421^{+0.012}_{-0.012}$	$16.669^{+0.003}_{-0.003}$	$3.179^{+0.011}_{-0.011}$	3.46	0	10
				$16.08^{+0.17}_{-0.16}$	$0.433^{+0.019}_{-0.019}$	$16.706^{+0.004}_{-0.004}$	$2.848^{+0.036}_{-0.038}$	3.63	0	
4FGL J0509.4+0542	TXS 0506+056	2018.10.06	0.14	$25.07^{+0.14}_{-0.13}$	$1.646^{+0.033}_{-0.033}$	$15.833^{+0.002}_{-0.002}$	$3.079^{+0.008}_{-0.008}$	9.13	0	23
				$23.86^{+0.11}_{-0.12}$	$1.529^{+0.029}_{-0.029}$	$15.816^{+0.002}_{-0.002}$	$3.359^{+0.014}_{-0.014}$	7.34	0	
		2017.10.03-2017.10.04	1.16	$13.30^{+0.10}_{-0.10}$	$1.040^{+0.025}_{-0.024}$	$16.493^{+0.003}_{-0.003}$	$3.819^{+0.046}_{-0.042}$	10.76	0.028	24
				$14.02^{+0.06}_{-0.06}$	$0.962^{+0.017}_{-0.017}$	$16.498^{+0.002}_{-0.002}$	$3.551^{+0.034}_{-0.038}$	9.83	0.023	
2017.10.31	1.16	$13.87^{+0.27}_{-0.31}$	$0.661^{+0.038}_{-0.047}$	$16.493^{+0.008}_{-0.010}$	$3.648^{+0.016}_{-0.016}$	9.97	0.029	24		
		$13.30^{+0.31}_{-0.35}$	$0.765^{+0.059}_{-0.057}$	$16.475^{+0.010}_{-0.011}$	$3.669^{+0.019}_{-0.020}$	9.97	0.028			
4FGL J0854.8+2006	OJ 287	2015.12.03	1.00	$14.92^{+0.07}_{-0.07}$	$0.899^{+0.017}_{-0.017}$	$16.471^{+0.002}_{-0.002}$	$3.107^{+0.029}_{-0.031}$	3.32	0	25
				$14.87^{+0.14}_{-0.09}$	$0.910^{+0.021}_{-0.028}$	$16.470^{+0.004}_{-0.003}$	$3.115^{+0.040}_{-0.036}$	3.07	0	
		2008.08.11-2008.11.11	10.70	$7.40^{+0.03}_{-0.03}$	$0.763^{+0.012}_{-0.011}$	$17.196^{+0.002}_{-0.002}$	$3.210^{+0.008}_{-0.008}$	2.17	0	26
				$7.78^{+0.03}_{-0.03}$	$0.961^{+0.017}_{-0.017}$	$17.218^{+0.002}_{-0.002}$	$3.157^{+0.007}_{-0.007}$	1.83	0	
		2009.10.20-2009.10.27	2.50	$10.16^{+0.12}_{-0.12}$	$0.492^{+0.026}_{-0.024}$	$16.702^{+0.005}_{-0.005}$	$3.261^{+0.059}_{-0.053}$	4.25	0	27
				$10.30^{+0.14}_{-0.14}$	$0.501^{+0.029}_{-0.028}$	$16.708^{+0.006}_{-0.005}$	$3.267^{+0.046}_{-0.043}$	4.02	0	
		2009.10.27-2009.11.17	2.50	$11.57^{+0.17}_{-0.17}$	$1.344^{+0.076}_{-0.070}$	$16.759^{+0.006}_{-0.006}$	$2.846^{+0.037}_{-0.034}$	3.04	0	27
				$12.81^{+1.66}_{-1.12}$	$1.925^{+1.594}_{-0.712}$	$16.803^{+0.053}_{-0.040}$	$2.375^{+0.534}_{-0.352}$	3.04	0	
		2009.11.17-2009.12.19	2.50	$11.11^{+0.19}_{-0.20}$	$1.821^{+0.111}_{-0.101}$	$16.741^{+0.007}_{-0.008}$	$2.832^{+0.035}_{-0.031}$	3.04	0	27
				$11.04^{+0.20}_{-0.19}$	$1.812^{+0.113}_{-0.110}$	$16.738^{+0.008}_{-0.008}$	$2.874^{+0.040}_{-0.041}$	3.04	0	

Note: Column (1) and (2) give the Fermi name and source name, respectively. The sources marked with * are the DT dominated LSPs with observed Doppler factors, and the others possess observed variability timescales. Column (3) gives the observed time period. Column (4) gives the observed or derived variability timescales. Column (5) gives the observed or derived Doppler factors. Column (6), (7) and (8) are the derived magnetic field strength, the derived radius of emission region and the derived break Lorentz factor of relativistic electrons, respectively. Column (9) and (10) give the lower limits of Doppler factors and distance between the black hole and emission region, which are derived from internal $\gamma\gamma$ absorption. Column (11) is the related reference. The table contains some rows with double sub-rows. The upper one is the parameter obtained by fitting SEDs with quadratic function, and the lower one is the parameter obtained by fitting SEDs with cubic function. References: (1) Sahakyan et al. 2020; (2) Ghisellini et al. 2010; (3) Tan et al. 2020; (4) Sahakyan et al. 2020; (5) Ammenadka et al. 2022; (6) Das, Mondal, and Prince 2023; (7) Palma et al. 2011; (8) Orienti et al. 2014; (9) Das, Prince, and Gupta 2020; (10) Roy et al. 2021; (11) Dutka et al. 2017; (12) D’Ammando et al. 2012; (13) Malik et al. 2022; (14) Patel et al. 2021; (15) Hayashida et al. 2015; (16) Fraija et al. 2019; (17) Zacharias et al. 2017; (18) Pacciani et al. 2014; (19) Gasparyan et al. 2018; (20) Prince et al. 2018; (21) Zacharias et al. 2019; (22) N. Sahakyan 2020; (23) Acciari et al. 2022; (24) Narek Sahakyan 2018; (25) Oikonomou et al. 2019; (26) Chen and Bai 2010; (27) Kushwaha, Sahayanathan, and Singh 2013.

- Abdo, A. A., M. Ackermann, M. Ajello, A. Allafort, E. Antolini, W. B. Atwood, M. Axelsson, L. Baldini, J. Ballet, G. Barbiellini, D. Bastieri, B. M. Baughman, K. Bechtol, R. Bellazzini, B. Berenji, et al. 2010. The First Catalog of Active Galactic Nuclei Detected by the Fermi Large Area Telescope. *ApJ* 715, no. 1 (May): 429–457. <https://doi.org/10.1088/0004-637X/715/1/429>. arXiv: 1002.0150 [astro-ph.HE].
- Abdo, A. A., M. Ackermann, M. Ajello, A. Allafort, L. Baldini, J. Ballet, G. Barbiellini, et al. 2011. Insights into the High-energy γ -ray Emission of Markarian 501 from Extensive Multifrequency Observations in the Fermi Era. *ApJ* 727, no. 2 (February): 129. <https://doi.org/10.1088/0004-637X/727/2/129>. arXiv: 1011.5260 [astro-ph.HE].
- Abdo, A. A., M. Ackermann, M. Ajello, E. Antolini, L. Baldini, J. Ballet, G. Barbiellini, et al. 2010. Gamma-ray Light Curves and Variability of Bright Fermi-detected Blazars. *ApJ* 722, no. 1 (October): 520–542. <https://doi.org/10.1088/0004-637X/722/1/520>. arXiv: 1004.0348 [astro-ph.HE].
- Acciari, V. A., T. Aniello, S. Ansoldi, L. A. Antonelli, A. Arbet Engels, M. Artero, K. Asano, et al. 2022. Investigating the Blazar TXS 0506+056 through Sharp Multiwavelength Eyes During 2017–2019. *ApJ* 927, no. 2 (March): 197. <https://doi.org/10.3847/1538-4357/ac531d>. arXiv: 2202.02600 [astro-ph.HE].
- Ackermann, M., M. Ajello, A. Albert, W. B. Atwood, L. Baldini, J. Ballet, G. Barbiellini, et al. 2016. Resolving the Extragalactic γ -Ray Background above 50 GeV with the Fermi Large Area Telescope. *Phys. Rev. Lett.* 116, no. 15 (April): 151105. <https://doi.org/10.1103/PhysRevLett.116.151105>. arXiv: 1511.00693 [astro-ph.CO].
- Agudo, I., S. G. Jorstad, A. P. Marscher, V. M. Larionov, J. L. Gómez, A. Lähteenmäki, M. Gurwell, et al. 2012. γ -ray emission region located in the parsec scale jet of OJ287. In *Journal of physics conference series*, 355:012032. Journal of Physics Conference Series. March. <https://doi.org/10.1088/1742-6596/355/1/012032>. arXiv: 1108.0925 [astro-ph.HE].
- Aguilar-Ruiz, E., N. Fraija, A. Galván-Gómez, and E. Benítez. 2022. A two-zone model as origin of hard TeV spectrum in extreme BL lacs. *MNRAS* 512, no. 2 (May): 1557–1566. <https://doi.org/10.1093/mnras/stac591>. arXiv: 2203.00880 [astro-ph.HE].
- Aharonian, F. A. 2000. TeV gamma rays from BL Lac objects due to synchrotron radiation of extremely high energy protons. *New A* 5, no. 7 (November): 377–395. [https://doi.org/10.1016/S1384-1076\(00\)00039-7](https://doi.org/10.1016/S1384-1076(00)00039-7). arXiv: astro-ph/0003159 [astro-ph].
- Ajello, M., D. Gasparrini, M. Sánchez-Conde, G. Zaharijas, M. Gustafsson, J. Cohen-Tanugi, C. D. Dermer, et al. 2015. The Origin of the Extragalactic Gamma-Ray Background and Implications for Dark Matter Annihilation. *ApJ* 800, no. 2 (February): L27. <https://doi.org/10.1088/2041-8205/800/2/L27>. arXiv: 1501.05301 [astro-ph.HE].
- Akaike, H. 1974. A New Look at the Statistical Model Identification. *IEEE Transactions on Automatic Control* 19 (January): 716–723.
- Almeyda, Triana, Andrew Robinson, Michael Richmond, Billy Vazquez, and Robert Nikutra. 2017. Modeling the Infrared Reverberation Response of the Circumnuclear Dusty Torus in AGNs: The Effects of Cloud Orientation and Anisotropic Illumination. *ApJ* 843, no. 1 (July): 3. <https://doi.org/10.3847/1538-4357/aa7687>. arXiv: 1709.07011 [astro-ph.GA].
- Ammenadka, Krishna Mohana, Debbijoy Bhattacharya, Subir Bhattacharyya, Nilay Bhatt, and Chelliah Subramonian Stalin. 2022. Long-Term Monitoring of Blazar PKS 0208–512: A Change of γ -Ray Baseline Activity from EGRET to Fermi Era. *Universe* 8, no. 10 (October): 534. <https://doi.org/10.3390/universe8100534>.
- Ansoldi, S., L. A. Antonelli, C. Arcaro, D. Baack, A. Babić, B. Banerjee, P. Bangale, et al. 2018. The Blazar TXS 0506+056 Associated with a High-energy Neutrino: Insights into Extragalactic Jets and Cosmic-Ray Acceleration. *ApJ* 863, no. 1 (August): L10. <https://doi.org/10.3847/2041-8213/aad083>. arXiv: 1807.04300 [astro-ph.HE].
- Arsioli, B., and Y. -L. Chang. 2018. The γ -ray emitting region in low synchrotron peak blazars. Testing self-synchrotron Compton and external Compton scenarios. *A&A* 616 (August): A63. <https://doi.org/10.1051/0004-6361/201833005>. arXiv: 1804.09761 [astro-ph.HE].
- Arsioli, B., and G. Polenta. 2018. A complete sample of LSP blazars fully described in γ -rays. New γ -ray detections and associations with Fermi-LAT. *A&A* 616 (August): A20. <https://doi.org/10.1051/0004-6361/201832786>. arXiv: 1804.03703 [astro-ph.HE].
- Bennett, C. L., D. Larson, J. L. Weiland, and G. Hinshaw. 2014. The 1% Concordance Hubble Constant. *ApJ* 794, no. 2 (October): 135. <https://doi.org/10.1088/0004-637X/794/2/135>. arXiv: 1406.1718 [astro-ph.CO].
- Bentz, Misty C., Bradley M. Peterson, Hagai Netzer, Richard W. Pogge, and Marianne Vestergaard. 2009. The Radius-Luminosity Relationship for Active Galactic Nuclei: The Effect of Host-Galaxy Starlight on Luminosity Measurements. II. The Full Sample of Reverberation-Mapped AGNs. *ApJ* 697, no. 1 (May): 160–181. <https://doi.org/10.1088/0004-637X/697/1/160>. arXiv: 0812.2283 [astro-ph].
- Błażejowski, M., M. Sikora, R. Moderski, and G. M. Madejski. 2000. Comptonization of Infrared Radiation from Hot Dust by Relativistic Jets in Quasars. *ApJ* 545, no. 1 (December): 107–116. <https://doi.org/10.1086/317791>. arXiv: astro-ph/0008154 [astro-ph].
- Blumenthal, George R., and Robert J. Gould. 1970. Bremsstrahlung, Synchrotron Radiation, and Compton Scattering of High-Energy Electrons Traversing Dilute Gases. *Reviews of Modern Physics* 42, no. 2 (January): 237–271. <https://doi.org/10.1103/RevModPhys.42.237>.
- Böttcher, M., A. Reimer, K. Sweeney, and A. Prakash. 2013. Leptonic and Hadronic Modeling of Fermi-detected Blazars. *ApJ* 768, no. 1 (May): 54. <https://doi.org/10.1088/0004-637X/768/1/54>. arXiv: 1304.0605 [astro-ph.HE].

- Böttcher, Markus, Charles D. Dermer, and Justin D. Finke. 2008. The Hard VHE γ -Ray Emission in High-Redshift TeV Blazars: Comptonization of Cosmic Microwave Background Radiation in an Extended Jet? *ApJ* 679, no. 1 (May): L9. <https://doi.org/10.1086/588780>. arXiv: 0804.3515 [astro-ph].
- Burnham, Kenneth P., and David R Anderson. 2002. *Model selection and multi-model inference: a practical information-theoretic approach*. Springer.
- Cao, Gang, and Jian-Cheng Wang. 2013. On the location of the γ -ray emission region for 21 flat spectrum radio quasars with quasi-simultaneous observations. *MNRAS* 436, no. 3 (December): 2170–2178. <https://doi.org/10.1093/mnras/stt1723>. arXiv: 1309.3206 [astro-ph.HE].
- Cerruti, M., A. Zech, C. Boisson, and S. Inoue. 2015. A hadronic origin for ultra-high-frequency-peaked BL Lac objects. *MNRAS* 448, no. 1 (March): 910–927. <https://doi.org/10.1093/mnras/stu2691>. arXiv: 1411.5968 [astro-ph.HE].
- Chen, Liang. 2014. Curvature of the Spectral Energy Distributions of Blazars. *ApJ* 788, no. 2 (June): 179. <https://doi.org/10.1088/0004-637X/788/2/179>. arXiv: 1405.1140 [astro-ph.HE].
- Chen, Liang, and Jin-Ming Bai. 2010. Is Low-Frequency-Peaked BL Lac Object OJ 287 a TeV Emitter? *Chinese Physics Letters* 27, no. 11 (November): 119501. <https://doi.org/10.1088/0256-307X/27/11/119501>. arXiv: 1009.2321 [astro-ph.CO].
- Coppi, P. S., and R. D. Blandford. 1990. Reaction rates and energy distributions for elementary processes in relativistic pair plasmas. *MNRAS* 245, no. 3 (August): 453–453. <https://doi.org/10.1093/mnras/245.3.453>.
- Costamante, L., G. Ghisellini, P. Giommi, G. Tagliaferri, A. Celotti, M. Chiaberge, L. Chiappetti, et al. 2001. New extreme synchrotron BL Lac objects. In *X-ray astronomy: stellar endpoints, agn, and the diffuse x-ray background*, edited by Nicholas E. White, Giuseppe Malaguti, and Giorgio G. C. Palumbo, 599:586–589. American Institute of Physics Conference Series. December. <https://doi.org/10.1063/1.1434692>. arXiv: astro-ph/0001410 [astro-ph].
- D’Ammando, F., A. Rau, P. Schady, J. Finke, M. Orienti, J. Greiner, D. A. Kann, et al. 2012. PKS 2123–463: a confirmed γ -ray blazar at high redshift. *MNRAS* 427, no. 1 (November): 893–900. <https://doi.org/10.1111/j.1365-2966.2012.22041.x>. arXiv: 1209.0479 [astro-ph.HE].
- Das, Avik Kumar, Sandeep Kumar Mondal, and Raj Prince. 2023. Gamma-ray flares and broad-band spectral study of PKS 0402–362. *MNRAS* 521, no. 3 (May): 3451–3474. <https://doi.org/10.1093/mnras/stad702>. arXiv: 2303.03039 [astro-ph.HE].
- Das, Avik Kumar, Raj Prince, and Nayantara Gupta. 2020. Gamma-Ray Flares in the Long-term Light Curve of 3C 454.3. *ApJS* 248, no. 1 (May): 8. <https://doi.org/10.3847/1538-4365/ab80c3>. arXiv: 2003.08266 [astro-ph.HE].
- Deng, Junhao, and Yunguo Jiang. 2023. Unravelling the secrets of blazar OT 081: a multiwavelength investigation. *MNRAS* 521, no. 4 (June): 6210–6218. <https://doi.org/10.1093/mnras/stad821>.
- Deng, Xue-Jiao, Rui Xue, Ze-Rui Wang, Shao-Qiang Xi, Hu-Bing Xiao, Lei-Ming Du, and Zhao-Hua Xie. 2021. The physical properties of γ -ray-quiet flat-spectrum radio quasars: why are they undetected by Fermi-LAT? *MNRAS* 506, no. 4 (October): 5764–5773. <https://doi.org/10.1093/mnras/stab2095>. arXiv: 2107.08757 [astro-ph.HE].
- Dermer, Charles D., Justin D. Finke, Hannah Krug, and Markus Böttcher. 2009. Gamma-Ray Studies of Blazars: Synchro-Compton Analysis of Flat Spectrum Radio Quasars. *ApJ* 692, no. 1 (February): 32–46. <https://doi.org/10.1088/0004-637X/692/1/32>. arXiv: 0808.3185 [astro-ph].
- Dermer, Charles D., and Govind Menon. 2009. *High Energy Radiation from Black Holes: Gamma Rays, Cosmic Rays, and Neutrinos*.
- Dermer, Charles D., and Reinhard Schlickeiser. 1993. Model for the High-Energy Emission from Blazars. *ApJ* 416 (October): 458. <https://doi.org/10.1086/173251>.
- Dondi, Laura, and Gabriele Ghisellini. 1995. Gamma-ray-loud blazars and beaming. *MNRAS* 273, no. 3 (April): 583–595. <https://doi.org/10.1093/mnras/273.3.583>.
- Dotson, Amanda, Markos Georganopoulos, Demosthenes Kazanas, and Eric S. Perlman. 2012. A Method for Localizing Energy Dissipation in Blazars Using Fermi Variability. *ApJ* 758, no. 1 (October): L15. <https://doi.org/10.1088/2041-8205/758/1/L15>. arXiv: 1209.2053 [astro-ph.HE].
- Dotson, Amanda, Markos Georganopoulos, Eileen T. Meyer, and Kevin McCann. 2015. On the Location of the 2009 GeV Flares of Blazar PKS 1510–089. *ApJ* 809, no. 2 (August): 164. <https://doi.org/10.1088/0004-637X/809/2/164>.
- Dutka, Michael S., Bryce D. Carpenter, Roopesh Ojha, Justin D. Finke, Filippo D’Ammando, Matthias Kadler, Philip G. Edwards, et al. 2017. Multiband Observations of the Quasar PKS 2326–502 during Active and Quiescent Gamma-Ray States in 2010–2012. *ApJ* 835, no. 2 (February): 182. <https://doi.org/10.3847/1538-4357/835/2/182>. arXiv: 1612.08061 [astro-ph.GA].
- Feng, Yaru, Shaoming Hu, Ruixin Zhou, and Songbo Gao. 2022. Explaining the Multiwavelength Emission of γ -ray Bright Flat-Spectrum Radio Quasar 3C 454.3 in Different Activity States. *Universe* 8, no. 11 (November): 585. <https://doi.org/10.3390/universe8110585>.
- Foffano, L., V. Vittorini, M. Tavani, and E. Menegoni. 2022. Absorption Features in Sub-TeV Gamma-Ray Spectra of BL Lac Objects. *ApJ* 926, no. 1 (February): 95. <https://doi.org/10.3847/1538-4357/ac46fc>. arXiv: 2201.02454 [astro-ph.HE].
- Foreman-Mackey, Daniel, David W. Hogg, Dustin Lang, and Jonathan Goodman. 2013. emcee: The MCMC Hammer. *PASP* 125, no. 925 (March): 306. <https://doi.org/10.1086/670067>. arXiv: 1202.3665 [astro-ph.IM].
- Fraija, N., E. Benítez, D. Hiriart, M. Sorcia, J. M. López, R. Mújica, J. I. Cabrera, and A. Galván-Gámez. 2019. Optical Polarimetric and Multiwavelength Flaring Activity of Blazar 3C 279. *ApJS* 245, no. 1 (November): 18. <https://doi.org/10.3847/1538-4365/ab3f28>. arXiv: 1908.08663 [astro-ph.HE].
- Gasparyan, S., N. Sahakyan, V. Baghmanyanyan, and D. Zargaryan. 2018. On the Multiwavelength Emission from CTA 102. *ApJ* 863, no. 2 (August): 114. <https://doi.org/10.3847/1538-4357/aad234>. arXiv: 1807.02869 [astro-ph.HE].
- Georganopoulos, M., E. T. Meyer, and G. Fossati. 2012. Using the SED to locate the Gamma-ray emission site of powerful blazars. *arXiv e-prints* (February): arXiv:1202.6193. <https://doi.org/10.48550/arXiv.1202.6193>. arXiv: 1202.6193 [astro-ph.HE].
- Ghisellini, G., and F. Tavecchio. 2008a. Rapid variability in TeV blazars: the case of PKS2155–304. *MNRAS* 386, no. 1 (May): L28–L32. <https://doi.org/10.1111/j.1745-3933.2008.00454.x>. arXiv: 0801.2569 [astro-ph].
- . 2008b. The blazar sequence: a new perspective. *MNRAS* 387, no. 4 (July): 1669–1680. <https://doi.org/10.1111/j.1365-2966.2008.13360.x>. arXiv: 0802.1918 [astro-ph].
- . 2009. Canonical high-power blazars. *MNRAS* 397, no. 2 (August): 985–1002. <https://doi.org/10.1111/j.1365-2966.2009.15007.x>. arXiv: 0902.0793 [astro-ph.CO].
- Ghisellini, G., F. Tavecchio, and M. Chiaberge. 2005. Structured jets in TeV BL Lac objects and radiogalaxies. Implications for the observed properties. *A&A* 432, no. 2 (March): 401–410. <https://doi.org/10.1051/0004-6361:20041404>. arXiv: astro-ph/0406093 [astro-ph].
- Ghisellini, G., F. Tavecchio, L. Foschini, G. Ghirlanda, L. Maraschi, and A. Celotti. 2010. General physical properties of bright Fermi blazars. *MNRAS* 402, no. 1 (February): 497–518. <https://doi.org/10.1111/j.1365-2966.2009.15898.x>. arXiv: 0909.0932 [astro-ph.CO].

- Ghisellini, Gabriele, and Piero Madau. 1996. On the origin of the gamma-ray emission in blazars. *MNRAS* 280, no. 1 (May): 67–76. <https://doi.org/10.1093/mnras/280.1.67>.
- Goodman, Jonathan, and Jonathan Weare. 2010. Ensemble samplers with affine invariance. *Communications in Applied Mathematics and Computational Science* 5, no. 1 (January): 65–80. <https://doi.org/10.2140/camcos.2010.5.65>.
- H. E. S. S. Collaboration, H. Abdalla, A. Abramowski, F. Aharonian, F. Ait Benkhali, A. G. Akhperjanian, T. Andersson, et al. 2017. Measurement of the EBL spectral energy distribution using the VHE γ -ray spectra of H.E.S.S. blazars. *A&A* 606 (October): A59. <https://doi.org/10.1051/0004-6361/201731200>. arXiv: 1707.06090 [astro-ph.HE].
- Harvey, Adam Leah W., Markos Georganopoulos, and Eileen T. Meyer. 2020. Powerful extragalactic jets dissipate their kinetic energy far from the central black hole. *Nature Communications* 11 (October): 5475. <https://doi.org/10.1038/s41467-020-19296-6>. arXiv: 2010.13670 [astro-ph.HE].
- Hayashida, M., G. M. Madejski, K. Nalewajko, M. Sikora, A. E. Wehrle, P. Ogle, W. Collmar, et al. 2012. The Structure and Emission Model of the Relativistic Jet in the Quasar 3C 279 Inferred from Radio to High-energy γ -Ray Observations in 2008–2010. *ApJ* 754, no. 2 (August): 114. <https://doi.org/10.1088/0004-637X/754/2/114>. arXiv: 1206.0745 [astro-ph.HE].
- Hayashida, M., K. Nalewajko, G. M. Madejski, M. Sikora, R. Itoh, M. Ajello, R. D. Blandford, et al. 2015. Rapid Variability of Blazar 3C 279 during Flaring States in 2013–2014 with Joint Fermi-LAT, NuSTAR, Swift, and Ground-Based Multiwavelength Observations. *ApJ* 807, no. 1 (July): 79. <https://doi.org/10.1088/0004-637X/807/1/79>. arXiv: 1502.04699 [astro-ph.HE].
- Hu, Hai-Bin, Hai-Qin Wang, Rui Xue, Fang-Kun Peng, and Ze-Rui Wang. 2024. The physical properties of Fermi-4LAC low-synchrotron-peaked BL Lac objects. *MNRAS* 528, no. 4 (March): 7587–7599. <https://doi.org/10.1093/mnras/stae522>. arXiv: 2402.10390 [astro-ph.HE].
- Hu, Wen, Ben-Zhong Dai, Wei Zeng, Zhong-Hui Fan, and Li Zhang. 2017. The properties of jet in luminous blazars under the equipartition condition. *New A* 52 (April): 82–95. <https://doi.org/10.1016/j.newast.2016.10.011>.
- Huang, Danyi, Ziyang Li, Jiru Liao, Xiulin Huang, Chengfeng Li, Yanjun Qian, Zhiyuan Pei, and Junhui Fan. 2022. Constraining the γ -Ray Emission Region for Fermi-detected FSRQs by the Seed Photon Approach. *PASP* 134, no. 1038 (August): 084102. <https://doi.org/10.1088/1538-3873/ac80d3>. arXiv: 2207.13058 [astro-ph.GA].
- IceCube Collaboration, M. G. Aartsen, M. Ackermann, J. Adams, J. A. Aguilar, M. Ahlers, M. Ahrens, et al. 2018. Multimessenger observations of a flaring blazar coincident with high-energy neutrino IceCube-170922A. *Science* 361, no. 6398 (July): eaat1378. <https://doi.org/10.1126/science.aat1378>. arXiv: 1807.08816 [astro-ph.HE].
- Jiang, Yunguo, Shao-Ming Hu, Xu Chen, Xi Shao, and Qiu-Hong Huo. 2020. Locations of optical and γ -ray emitting regions and variation phenomena of PMN J2345–1555. *MNRAS* 493, no. 3 (April): 3757–3769. <https://doi.org/10.1093/mnras/staa475>. arXiv: 1809.04984 [astro-ph.HE].
- Kaspi, Shai, W. N. Brandt, Dan Maoz, Hagai Netzer, Donald P. Schneider, and Ohad Shemmer. 2007. Reverberation Mapping of High-Luminosity Quasars: First Results. *ApJ* 659, no. 2 (April): 997–1007. <https://doi.org/10.1086/512094>. arXiv: astro-ph/0612722 [astro-ph].
- Kushwaha, Pankaj, S. Sahayanathan, and K. P. Singh. 2013. High energy emission processes in OJ 287 during 2009 flare. *MNRAS* 433, no. 3 (August): 2380–2388. <https://doi.org/10.1093/mnras/stt904>. arXiv: 1305.5065 [astro-ph.HE].
- Li, Wei-Jian, Rui Xue, Guang-Bo Long, Ze-Rui Wang, Shigehiro Nagataki, Da-Hai Yan, and Jian-Cheng Wang. 2022. Can the one-zone hadronuclear model explain the hard-TeV spectrum of BL Lac objects? *A&A* 659 (March): A184. <https://doi.org/10.1051/0004-6361/202142051>. arXiv: 2201.12708 [astro-ph.HE].
- Liodakis, Ioannis, Talvikki Hovatta, Daniela Huppenkothen, Sebastian Kiehlmann, Walter Max-Moerbeck, and Anthony C. S. Readhead. 2018. Constraining the Limiting Brightness Temperature and Doppler Factors for the Largest Sample of Radio-bright Blazars. *ApJ* 866, no. 2 (October): 137. <https://doi.org/10.3847/1538-4357/aae2b7>. arXiv: 1809.08249 [astro-ph.HE].
- Lopez-Rodriguez, Enrique, Lindsay Fuller, Almudena Alonso-Herrero, Andreas Efstathiou, Kohei Ichikawa, Nancy A. Levenson, Chris Packham, et al. 2018. The Emission and Distribution of Dust of the Torus of NGC 1068. *ApJ* 859, no. 2 (June): 99. <https://doi.org/10.3847/1538-4357/aabd7b>. arXiv: 1804.04134 [astro-ph.GA].
- Lyu, Jianwei, and George H. Rieke. 2018. Polar Dust, Nuclear Obscuration, and IR SED Diversity in Type-1 AGNs. *ApJ* 866, no. 2 (October): 92. <https://doi.org/10.3847/1538-4357/aae075>. arXiv: 1809.03080 [astro-ph.GA].
- Macomb, D. J., C. W. Akerlof, H. D. Aller, M. F. Aller, D. L. Bertsch, F. Bruhweiler, J. H. Buckley, et al. 1995. Multiwavelength Observations of Markarian 421 During a TeV/X-Ray Flare. *ApJ* 449 (August): L99. <https://doi.org/10.1086/309646>.
- Madejski, Grzegorz (Greg), and Marek Sikora. 2016. Gamma-Ray Observations of Active Galactic Nuclei. *ARA&A* 54 (September): 725–760. <https://doi.org/10.1146/annurev-astro-081913-040044>.
- Malik, Zahoor, Zahir Shah, Sunder Sahayanathan, Naseer Iqbal, and Aaqib Manzoor. 2022. Multiwavelength study of blazar 4C + 01.02 during its long-term flaring activity in 2014–2017. *MNRAS* 514, no. 3 (August): 4259–4269. <https://doi.org/10.1093/mnras/stac1616>. arXiv: 2206.04441 [astro-ph.HE].
- Maraschi, L., G. Ghisellini, and A. Celotti. 1992. A Jet Model for the Gamma-Ray-emitting Blazar 3C 279. *ApJ* 397 (September): L5. <https://doi.org/10.1086/186531>.
- Marscher, A. P., and W. K. Gear. 1985. Models for high-frequency radio outbursts in extragalactic sources, with application to the early 1983 millimeter-to-infrared flare of 3C 273. *ApJ* 298 (November): 114–127. <https://doi.org/10.1086/163592>.
- Moderski, Rafał, Marek Sikora, Paolo S. Coppi, and Felix Aharonian. 2005. Klein-Nishina effects in the spectra of non-thermal sources immersed in external radiation fields. *MNRAS* 363, no. 3 (November): 954–966. <https://doi.org/10.1111/j.1365-2966.2005.09494.x>. arXiv: astro-ph/0504388 [astro-ph].
- Nalewajko, Krzysztof, Mitchell C. Begelman, and Marek Sikora. 2014. Constraining the Location of Gamma-Ray Flares in Luminous Blazars. *ApJ* 789, no. 2 (July): 161. <https://doi.org/10.1088/0004-637X/789/2/161>. arXiv: 1405.7694 [astro-ph.HE].
- Oikonomou, Foteini, Kohta Murase, Paolo Padovani, Elisa Resconi, and Peter Mészáros. 2019. High-energy neutrino flux from individual blazar flares. *MNRAS* 489, no. 3 (November): 4347–4366. <https://doi.org/10.1093/mnras/stz2246>. arXiv: 1906.05302 [astro-ph.HE].
- Orienti, M., F. D’Ammando, M. Giroletti, J. Finke, M. Ajello, D. Dallacasa, and T. Venturi. 2014. Exploring the multiband emission of TXS 0536+145: the most distant γ -ray flaring blazar. *MNRAS* 444, no. 4 (November): 3040–3051. <https://doi.org/10.1093/mnras/stu1644>. arXiv: 1409.0392 [astro-ph.HE].
- Pacciani, L., F. Tavecchio, I. Donnarumma, A. Stamerra, L. Carrasco, E. Recillas, A. Porras, and M. Uemura. 2014. Exploring the Blazar Zone in High-energy Flares of FSRQs. *ApJ* 790, no. 1 (August): 45. <https://doi.org/10.1088/0004-637X/790/1/45>. arXiv: 1312.3998 [astro-ph.HE].

- Padovani, P., P. Giommi, E. Resconi, T. Glauch, B. Arsioli, N. Sahakyan, and M. Huber. 2018. Dissecting the region around IceCube-170922A: the blazar TXS 0506+056 as the first cosmic neutrino source. *MNRAS* 480, no. 1 (October): 192–203. <https://doi.org/10.1093/mnras/sty1852>. arXiv: 1807.04461 [astro-ph.HE].
- Padovani, Paolo, and Paolo Giommi. 1995. The Connection between X-Ray- and Radio-selected BL Lacertae Objects. *ApJ* 444 (May): 567. <https://doi.org/10.1086/175631>. arXiv: astro-ph/9412073 [astro-ph].
- Palma, N. I., M. Böttcher, I. de la Calle, I. Agudo, M. Aller, H. Aller, U. Bach, et al. 2011. Multiwavelength Observations of the Gamma-Ray Blazar PKS 0528+134 in Quiescence. *ApJ* 735, no. 1 (July): 60. <https://doi.org/10.1088/0004-637X/735/1/60>. arXiv: 1104.3557 [astro-ph.HE].
- Patel, S. R., D. Bose, N. Gupta, and M. Zuberi. 2021. Broadband modelling of Orphan gamma ray flares. *Journal of High Energy Astrophysics* 29 (March): 31–39. <https://doi.org/10.1016/j.jheap.2020.12.001>. arXiv: 2012.10291 [astro-ph.HE].
- Patiño-Álvarez, V. M., S. Fernandes, V. Chavushyan, E. López-Rodríguez, J. León-Tavares, E. M. Schlegel, L. Carrasco, J. Valdés, and A. Carrafiñana. 2018. Multiwavelength photometric and spectropolarimetric analysis of the FSRQ 3C 279. *MNRAS* 479, no. 2 (September): 2037–2064. <https://doi.org/10.1093/mnras/sty1497>. arXiv: 1806.01693 [astro-ph.HE].
- Pei, Zhiyuan, Junhui Fan, Jianghe Yang, Danyi Huang, and Ziyang Li. 2022. The Estimation of Fundamental Physics Parameters for Fermi-LAT Blazars. *ApJ* 925, no. 1 (January): 97. <https://doi.org/10.3847/1538-4357/ac3aeb>. arXiv: 2112.00530 [astro-ph.HE].
- Potter, William J., and Garret Cotter. 2013a. Synchrotron and inverse-Compton emission from blazar jets – II. An accelerating jet model with a geometry set by observations of M87. *MNRAS* 429, no. 2 (February): 1189–1205. <https://doi.org/10.1093/mnras/sts407>. arXiv: 1212.2632 [astro-ph.HE].
- . 2013b. Synchrotron and inverse-Compton emission from blazar jets – III. Compton-dominant blazars. *MNRAS* 431, no. 2 (May): 1840–1852. <https://doi.org/10.1093/mnras/stt300>. arXiv: 1303.1182 [astro-ph.HE].
- . 2013c. Synchrotron and inverse-Compton emission from blazar jets – IV. BL Lac type blazars and the physical basis for the blazar sequence. *MNRAS* 436, no. 1 (November): 304–314. <https://doi.org/10.1093/mnras/stt1569>. arXiv: 1310.0462 [astro-ph.HE].
- Prince, Raj, Gayathri Raman, Joachim Hahn, Nayantara Gupta, and Pratik Majumdar. 2018. Fermi-Large Area Telescope Observations of the Brightest Gamma-Ray Flare Ever Detected from CTA 102. *ApJ* 866, no. 1 (October): 16. <https://doi.org/10.3847/1538-4357/aadadb>. arXiv: 1808.05027 [astro-ph.HE].
- Roy, Abhradeep, S. R. Patel, A. Sarkar, A. Chatterjee, and V. R. Chitnis. 2021. Multiwavelength study of the quiescent states of six brightest flat-spectrum radio quasars detected by Fermi-LAT. *MNRAS* 504, no. 1 (June): 1103–1114. <https://doi.org/10.1093/mnras/stab975>. arXiv: 2104.08566 [astro-ph.HE].
- Rybicki, G. B., A. P. Lightman, and R. J. Tayler. 1981. Book-Review - Radiative Processes in Astrophysics. *Nature* 289 (February): 729.
- Sahakyan, N. 2020. Investigation of the γ -ray spectrum of CTA 102 during the exceptional flaring state in 2016–2017. *A&A* 635 (March): A25. <https://doi.org/10.1051/0004-6361/201936715>. arXiv: 1911.12087 [astro-ph.HE].
- Sahakyan, N., D. Israyelyan, G. Harutyunyan, M. Khachatryan, and S. Gasparian. 2020. Multiwavelength study of high-redshift blazars. *MNRAS* 498, no. 2 (October): 2594–2613. <https://doi.org/10.1093/mnras/staa2477>. arXiv: 2008.09675 [astro-ph.HE].
- Sahakyan, Narek. 2018. Lepto-hadronic γ -Ray and Neutrino Emission from the Jet of TXS 0506+056. *ApJ* 866, no. 2 (October): 109. <https://doi.org/10.3847/1538-4357/aadade>. arXiv: 1808.05651 [astro-ph.HE].
- Shukla, A., V. R. Chitnis, B. B. Singh, B. S. Acharya, G. C. Anupama, P. Bhattacharjee, R. J. Britto, et al. 2015. Multi-frequency, Multi-epoch Study of Mrk 501: Hints for a Two-component Nature of the Emission. *ApJ* 798, no. 1 (January): 2. <https://doi.org/10.1088/0004-637X/798/1/2>. arXiv: 1503.02706 [astro-ph.HE].
- Sikora, Marek, Mitchell C. Begelman, and Martin J. Rees. 1994. Comptonization of Diffuse Ambient Radiation by a Relativistic Jet: The Source of Gamma Rays from Blazars? *ApJ* 421 (January): 153. <https://doi.org/10.1086/173633>.
- Sikora, Marek, Rafał Moderski, and Greg M. Madejski. 2008. 3C 454.3 Reveals the Structure and Physics of Its “Blazar Zone”. *ApJ* 675, no. 1 (March): 71–78. <https://doi.org/10.1086/526419>. arXiv: 0711.3524 [astro-ph].
- Speagle, Joshua S. 2019. A Conceptual Introduction to Markov Chain Monte Carlo Methods. *arXiv e-prints* (September): arXiv:1909.12313. <https://doi.org/10.48550/arXiv.1909.12313>. arXiv: 1909.12313 [stat.OT].
- Tan, Can, Rui Xue, Lei-Ming Du, Shao-Qiang Xi, Ze-Rui Wang, and Zhao-Hua Xie. 2020. The Physical Properties of Fermi-4LAC Flat Spectrum Radio Quasars. *ApJS* 248, no. 2 (June): 27. <https://doi.org/10.3847/1538-4365/ab8cc6>. arXiv: 2005.09553 [astro-ph.HE].
- Tavecchio, F., and G. Ghisellini. 2014. On the spine-layer scenario for the very high-energy emission of NGC 1275. *MNRAS* 443, no. 2 (September): 1224–1230. <https://doi.org/10.1093/mnras/stu1196>. arXiv: 1404.6894 [astro-ph.HE].
- Tavecchio, F., G. Ghisellini, G. Bonnoli, and G. Ghirlanda. 2010. Constraining the location of the emitting region in Fermi blazars through rapid γ -ray variability. *MNRAS* 405, no. 1 (June): L94–L98. <https://doi.org/10.1111/j.1745-3933.2010.00867.x>. arXiv: 1003.3475 [astro-ph.CO].
- Tavecchio, Fabrizio, and Gabriele Ghisellini. 2008. The spectrum of the broad-line region and the high-energy emission of powerful blazars. *MNRAS* 386, no. 2 (May): 945–952. <https://doi.org/10.1111/j.1365-2966.2008.13072.x>. arXiv: 0802.0871 [astro-ph].
- Tavecchio, Fabrizio, Laura Maraschi, and Gabriele Ghisellini. 1998. Constraints on the Physical Parameters of TeV Blazars. *ApJ* 509, no. 2 (December): 608–619. <https://doi.org/10.1086/306526>. arXiv: astro-ph/9809051 [astro-ph].
- Urry, C. Megan, and Paolo Padovani. 1995. Unified Schemes for Radio-Loud Active Galactic Nuclei. *PASP* 107 (September): 803. <https://doi.org/10.1086/133630>. arXiv: astro-ph/9506063 [astro-ph].
- Wu, Linhui, Qingwen Wu, Dahai Yan, Liang Chen, and Xuliang Fan. 2018. Constraints on the Location of γ -Ray Sample of Blazars with Radio Core-shift Measurements. *ApJ* 852, no. 1 (January): 45. <https://doi.org/10.3847/1538-4357/aa9b7e>. arXiv: 1711.05889 [astro-ph.HE].
- Xue, R., D. Luo, L. M. Du, Z. R. Wang, Z. H. Xie, T. F. Yi, D. R. Xiong, Y. B. Xu, W. G. Liu, and X. L. Yu. 2016. Curvature of the spectral distribution, the inverse Compton component and the jet in Fermi 2LAC blazars. *MNRAS* 463, no. 3 (December): 3038–3055. <https://doi.org/10.1093/mnras/stw2038>. arXiv: 1609.05697 [astro-ph.HE].
- Xue, Rui, Ruo-Yu Liu, Ze-Rui Wang, Nan Ding, and Xiang-Yu Wang. 2021. A Two-zone Blazar Radiation Model for “Orphan” Neutrino Flares. *ApJ* 906, no. 1 (January): 51. <https://doi.org/10.3847/1538-4357/abc886>. arXiv: 2011.03681 [astro-ph.HE].
- Xue, Rui, Ze-Rui Wang, and Wei-Jian Li. 2022. Hadronuclear interactions in the jet of low TeV luminosity AGN: Implications for the low-state very-high-energy gamma-ray emission. *Phys. Rev. D* 106, no. 10 (November): 103021. <https://doi.org/10.1103/PhysRevD.106.103021>. arXiv: 2210.09797 [astro-ph.HE].
- Yamada, Yurika, Makoto Uemura, Ryosuke Itoh, Yasushi Fukazawa, Masanori Ohno, and Fumiya Imazato. 2020. Variations of the physical parameters of the blazar Mrk 421 based on analysis of the spectral energy distributions. *PASJ* 72, no. 3 (June): 42. <https://doi.org/10.1093/pasj/psaa028>. arXiv: 2003.08016 [astro-ph.HE].

- Yan, Dahai, Qingwen Wu, Xuliang Fan, Jiancheng Wang, and Li Zhang. 2018. A Method for Locating a High-energy Dissipation Region in a Blazar. *ApJ* 859, no. 2 (June): 168. <https://doi.org/10.3847/1538-4357/aac20a>. arXiv: 1711.05939 [astro-ph.HE].
- Yang, J. H., J. H. Fan, Y. Liu, M. X. Tuo, Z. Y. Pei, W. X. Yang, Y. H. Yuan, et al. 2022. The Spectral Energy Distributions for 4FGL Blazars. *ApJS* 262, no. 1 (September): 18. <https://doi.org/10.3847/1538-4365/ac7deb>.
- Yang, J. H., J. H. Fan, Y. Liu, M. X. Tuo, Z. Y. Pei, W. X. Yang, Y. H. Yuan, et al. 2023. Estimation of inverse Compton peak frequency for 4FGL Blazars. *Science China Physics, Mechanics, and Astronomy* 66, no. 4 (April): 249511. <https://doi.org/10.1007/s11433-022-2062-2>.
- Zacharias, M., M. Böttcher, F. Jankowsky, J. -P. Lenain, S. J. Wagner, and A. Wiercholska. 2017. Cloud Ablation by a Relativistic Jet and the Extended Flare in CTA 102 in 2016 and 2017. *ApJ* 851, no. 2 (December): 72. <https://doi.org/10.3847/1538-4357/aa9bee>. arXiv: 1711.06117 [astro-ph.HE].
- . 2019. The Extended Flare in CTA 102 in 2016 and 2017 within a Hadronic Model through Cloud Ablation by the Relativistic Jet. *ApJ* 871, no. 1 (January): 19. <https://doi.org/10.3847/1538-4357/aaf4f7>. arXiv: 1811.12299 [astro-ph.HE].
- Zhang, Lixia, Xiaobiao Chen, Shihui He, Wenwen Nie, Wentao Tang, Jiawei Huang, Guohai Chen, and Junhui Fan. 2024. Jet Mechanism and γ -Ray-emitting Region for Fermi Flat-spectrum Radio Quasars with Broad-line Emissions. *ApJS* 271, no. 1 (March): 27. <https://doi.org/10.3847/1538-4365/ad20c8>.

Appendix 1. SED Fitting Results

Figures 7 to 12 present all the 45 SEDs fitted by both quadratic and cubic functions. A and B denote the SEDs fitted by quadratic and cubic functions, respectively. Blue and light blue scatters represent the simultaneous and archival data, respectively. Black lines are plotted using the maximum posterior values. Yellow areas denote the $1\text{-}\sigma$ uncertainties under 16–50–84 rule. The AICc of each hump and observed seed factors are displayed on the figures.

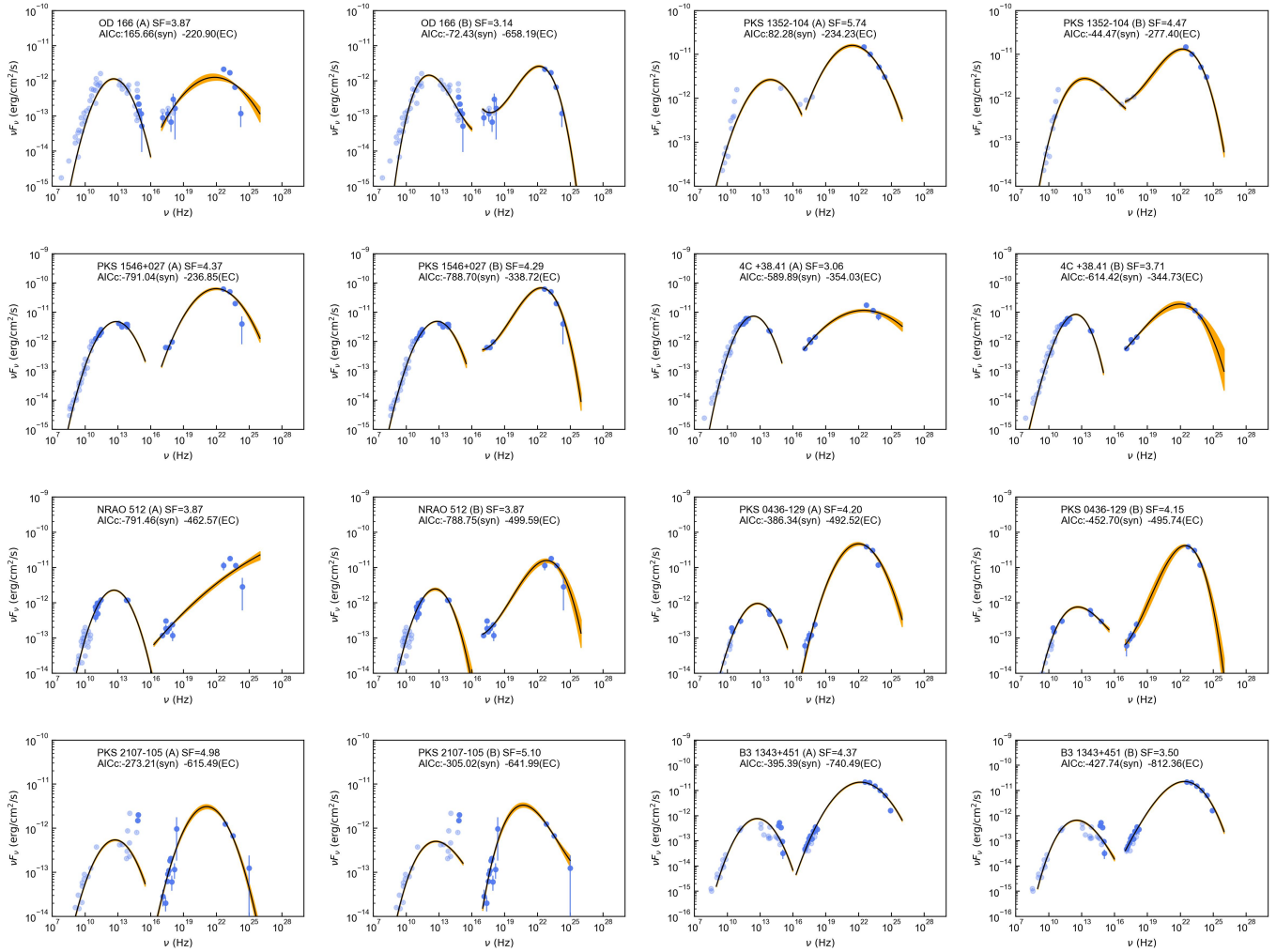


Figure 7. SED fitting results of the blazars dominated by dusty torus with Doppler factors.

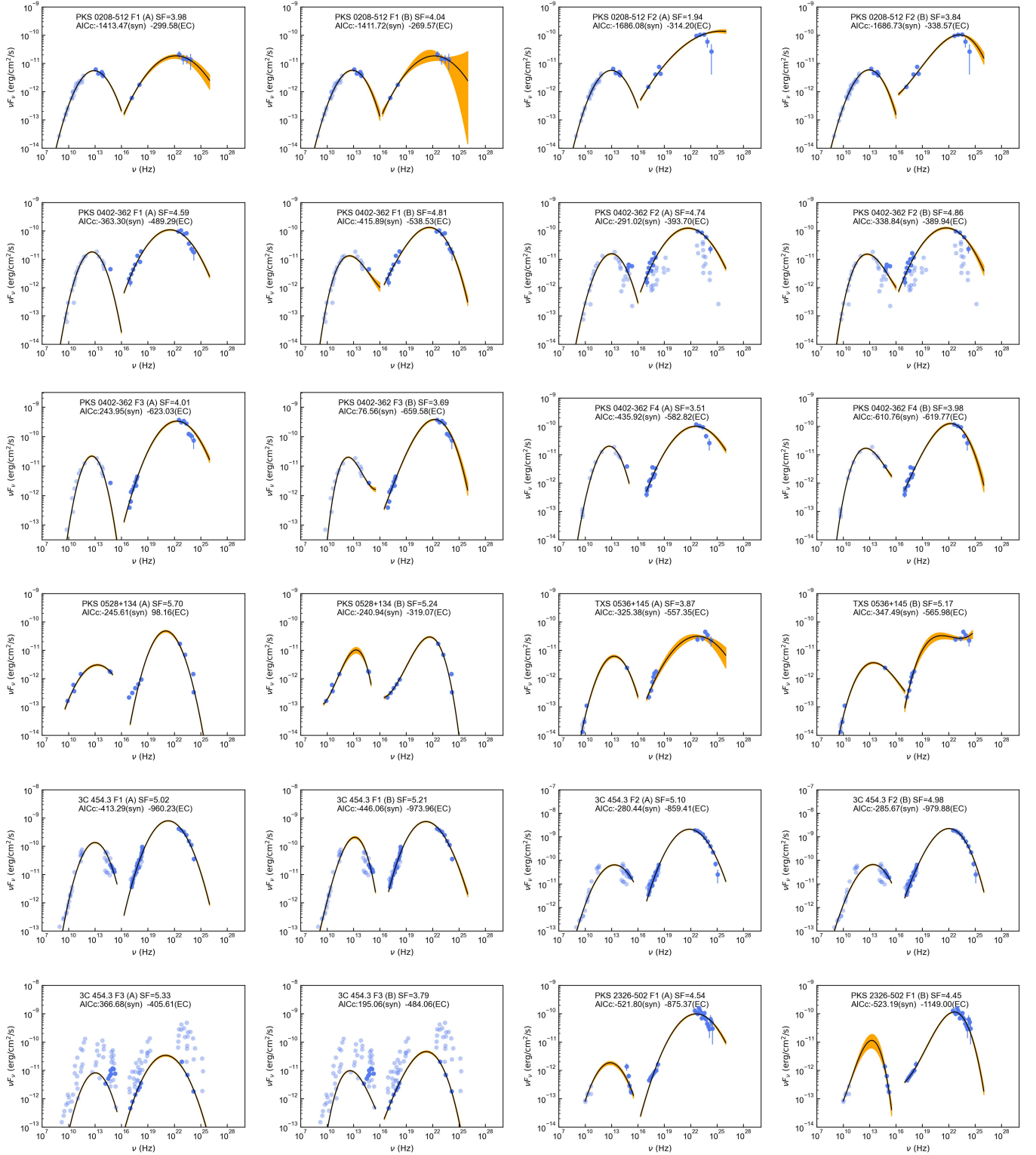


Figure 8. SED fitting results of the blazars dominated by dusty torus with variability timescales.

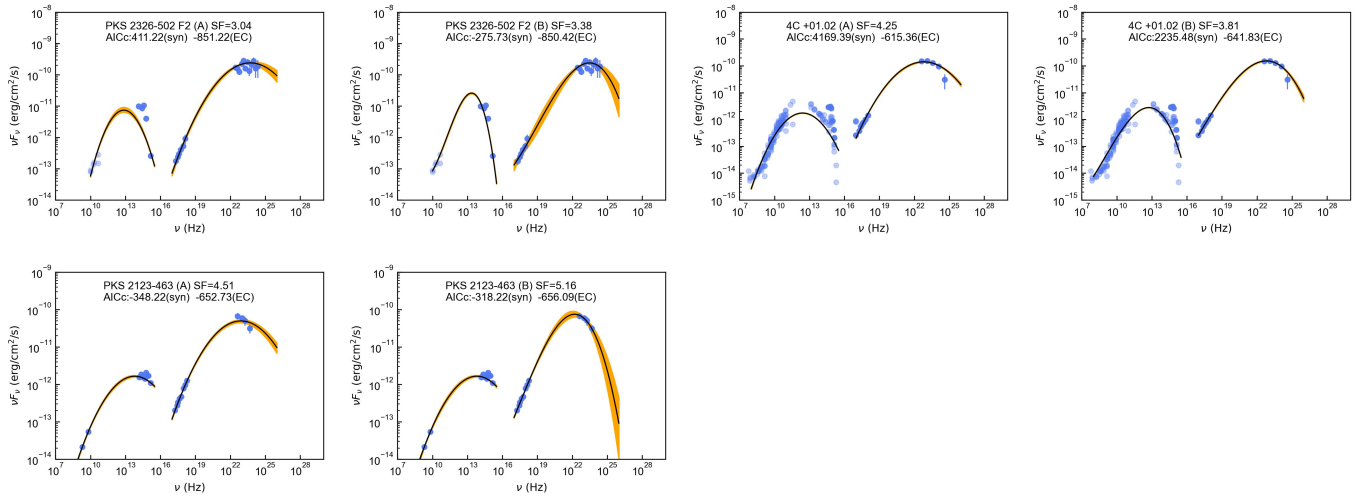


Figure 8. SED fitting results of the blazars dominated by dusty torus with variability timescales.

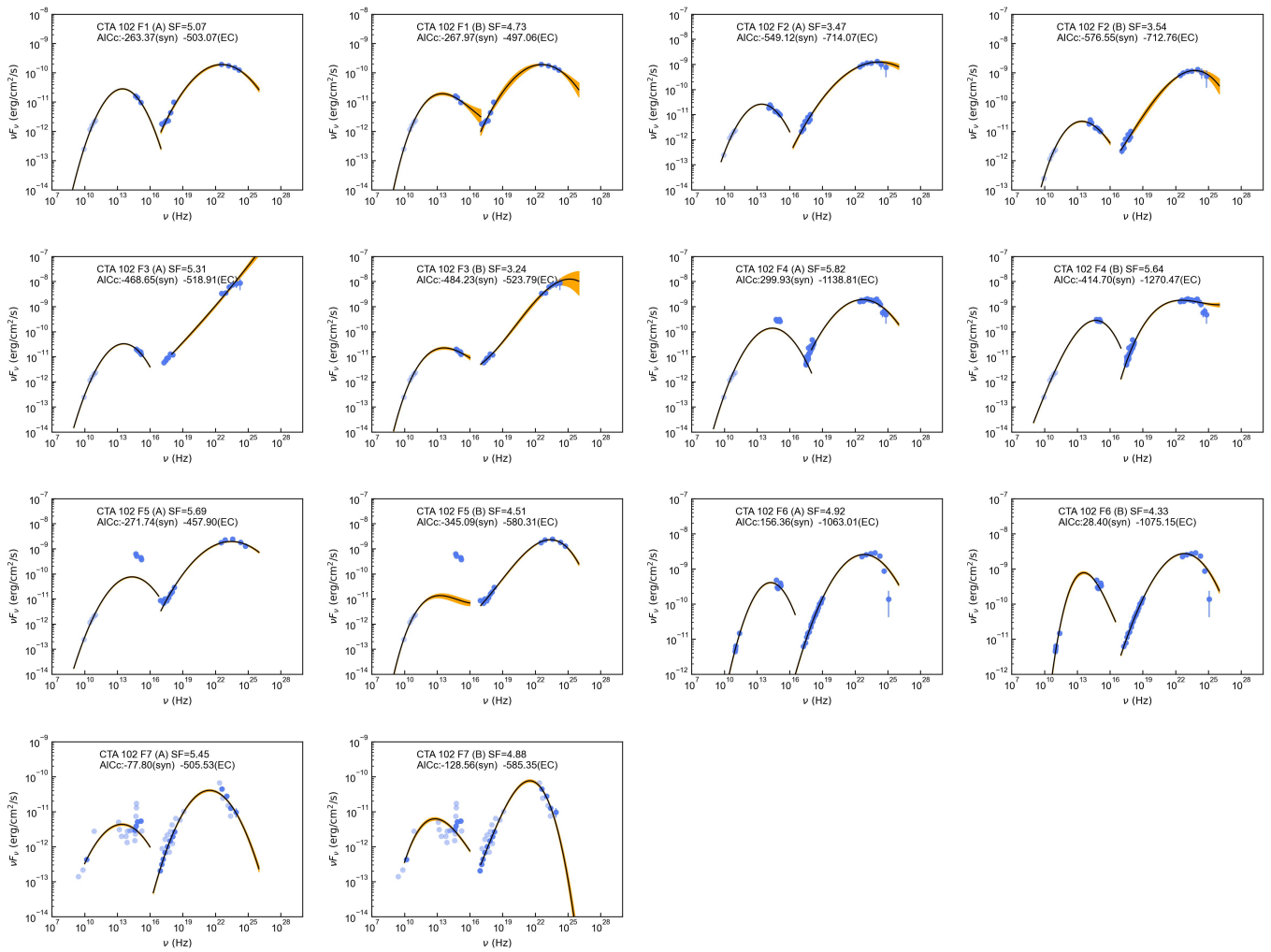


Figure 9. SED fitting results of CTA 102.

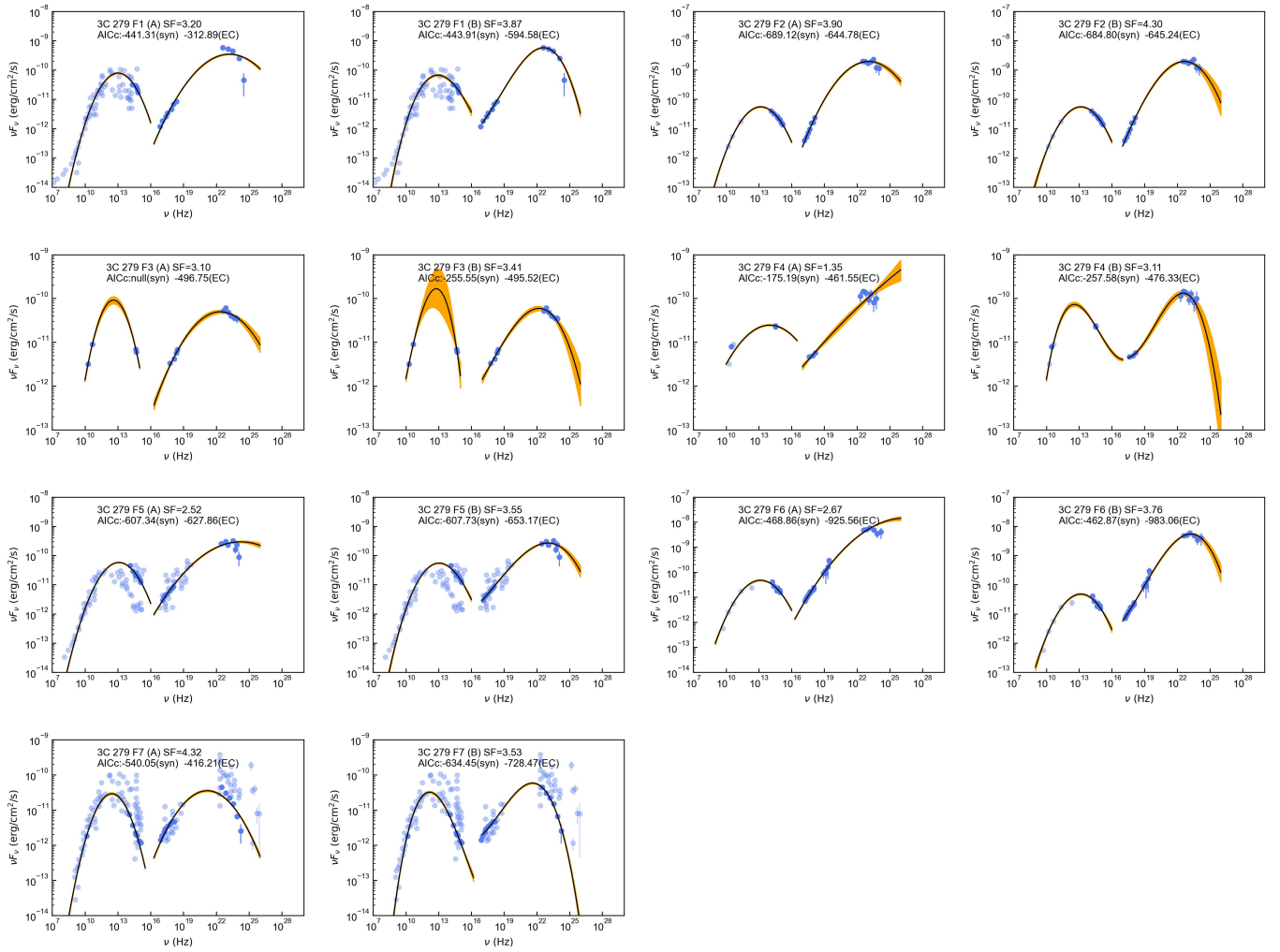


Figure 10. SED fitting results of 3C 279.

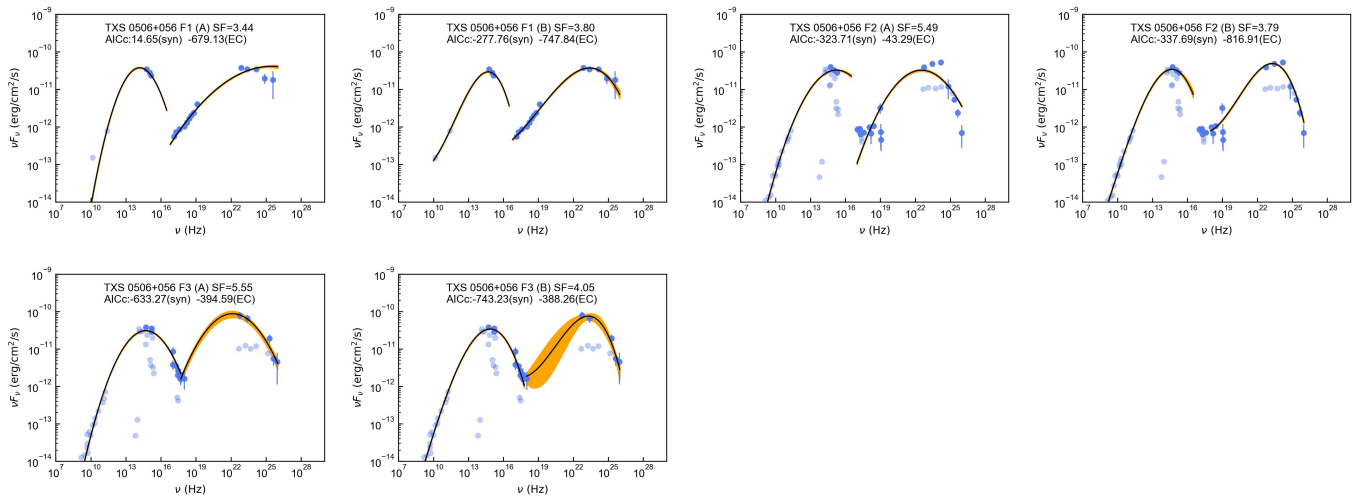


Figure 11. SED fitting results of TXS 0506+056.

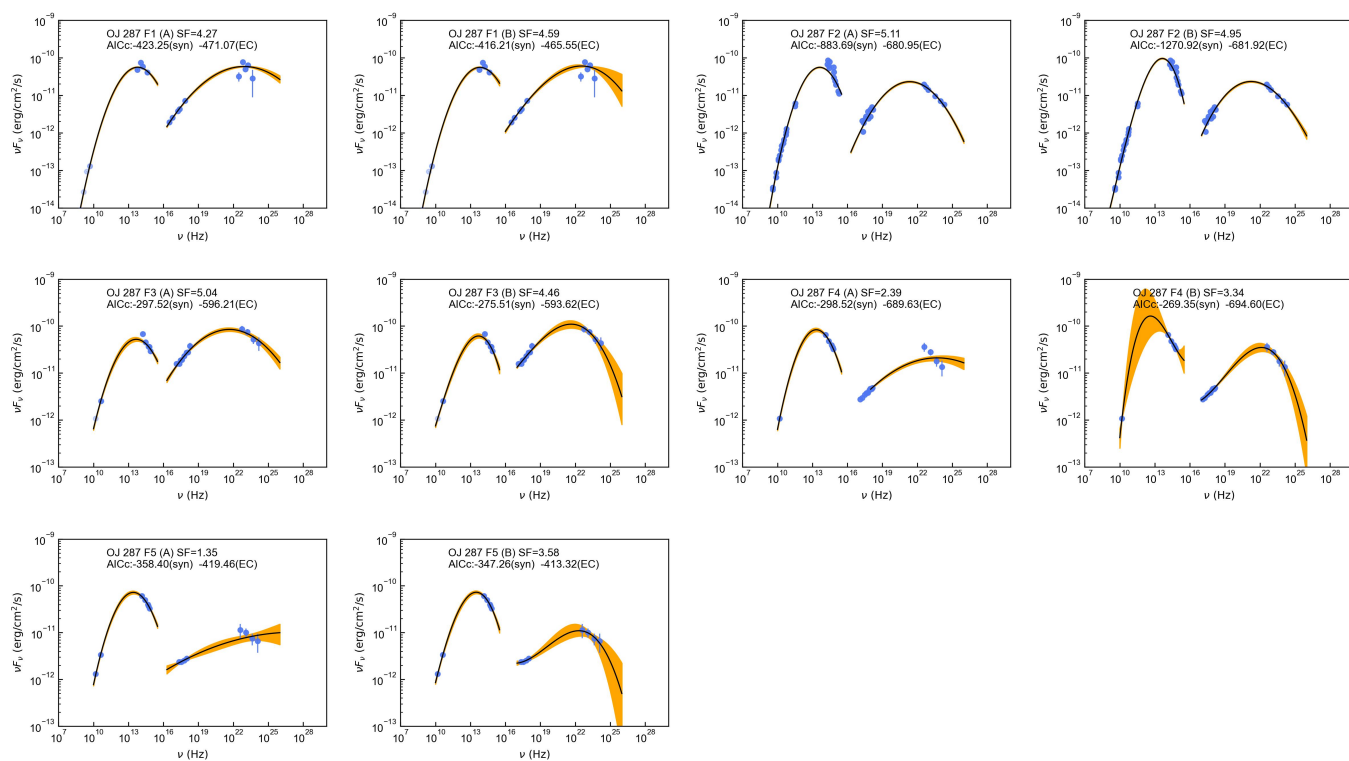


Figure 12. SED fitting results of OJ 287.